Featured in Physics

Engineered Molecular Clock Transitions for Precision Measurements

Yuiki Takahashi,[*] Harish D. Ramachandran,[†] Arian Jadbabaie,[‡] Yi Zeng,[§] Chi Zhang, and Nicholas R. Hutzler

Division of Physics, Mathematics, and Astronomy, California Institute of Technology, Pasadena, California 91125, USA

(Received 8 October 2025; accepted 28 April 2026; published 20 July 2026)

Heavy polar molecules are sensitive probes of physics beyond the standard model. However, uncontrolled external electromagnetic fields pose challenges to achieving precise and accurate measurements. Minimizing susceptibility to these fields is therefore critical and has played an important role in all precision experiments of this type. Here we devise and demonstrate clock transitions engineered to realize robust symmetry violation searches in the polyatomic molecule YbOH. Sensitivities to external fields can be suppressed by orders of magnitude while preserving high sensitivity to the electron electric dipole moment. We perform Ramsey measurements on these clock transitions and observe suppression of electric and magnetic sensitivities by at least factors of 700 and 200, respectively, and demonstrate the robustness of their spin coherence against large electromagnetic-field fluctuations. We further identify and employ selected quantum states to make sensitive measurements of external magnetic and electric fields, another critical feature for highly accurate measurements. This approach of molecular engineering is broadly applicable to diverse molecular species and states, including those with complex nuclei and those that are compatible with state-of-the-art cooling and trapping techniques, thereby offering the potential to significantly improve experimental sensitivity to a wide range of new physics while expanding the chemical design space for molecular quantum science.

DOI: 10.1103/4t7q-d58r

Subject Areas: Atomic and Molecular Physics, Particles and Fields, Quantum Physics

I. INTRODUCTION

Molecules are emerging as versatile quantum platforms with transformative applications in quantum information and simulation, ultracold chemistry, precision metrology, and fundamental physics, owing to their rich internal structures, long coherence times, and long-range interactions [1–3]. In particular, heavy polar molecules are powerful quantum sensors for probing physics beyond the standard model (BSM) [3–6]. An especially promising route is searching for electromagnetic moments whose nonzero value would indicate time (T) and charge-parity (CP) symmetry violation, such as the electron electric dipole moment (eEDM) [5]. The most sensitive eEDM searches, performed with HfF^+ [7] and ThO [8], probe fundamental new physics at energies of around tens of TeV, well beyond the reach of the near-term particle colliders. These experiments achieve high sensitivity by leveraging the enhancement of CP-violating effects due to the large internal electric field in heavy polar molecules combined with two key advantages of a $^3\Delta_1$ molecular state. First, these states have a reduced magnetic moment of approximately $0.01\mu_B$, where μ_B is the Bohr magneton, which minimizes sensitivity to unwanted magnetic-field effects [9]. Second, these states can be polarized in small electric fields $\lesssim$10 V/cm and give rise to "internal comagnetometers," which enable reversal of the eEDM-induced energy shifts independent of the laboratory fields [10]. Nevertheless, residual sensitivities to uncontrolled fields remain a critical challenge, giving rise to systematic shifts that can mimic an eEDM signal. Consequently, both experiments require careful measures to correct and reject these effects, and rely very heavily on the intrinsic reduced sensitivity and comagnetometry offered by the $^3\Delta_1$ state.

Combining modern quantum tools with molecular CP-violation searches offers the potential to improve sensitivities to new physics by orders of magnitude, reaching PeV energy scales [11]. The most sensitive EDM experiments rely on the $^3\Delta_1$ structure, but such a structure

[*]Contact author: yuiki@caltech.edu

[†]Present address: Department of Physics, The Johns Hopkins University, Baltimore, Maryland 21218, USA.

[‡]Present address: Department of Physics, Massachusetts Institute of Technology, Cambridge, Massachusetts 02139, USA.

[§]Present address: Institut für Experimentalphysik, Universität Innsbruck, A-6020 Innsbruck, Austria.

is generally not compatible with optical cycling or ultracold assembly—mainstay techniques that could dramatically enhance experimental sensitivity, especially for neutral species. Laser-coolable molecules typically feature a $^2\Sigma$ structure arising from a single, metal-centered valence electron [12–14], and as a result have magnetic moments on the order of approximately μ_B, which is roughly 100 times larger than that of the $^3\Delta_1$ state. This makes it challenging to utilize laser-coolable molecules for *CP*-violation searches given that stray electromagnetic fields remain a primary source of systematic errors [15]. Additionally, molecules used to search for nuclear *CP* violation typically have very complicated hyperfine structure [16,17], making demonstrated methods largely inapplicable. While there are methods to overcome some of these challenges [18–20], they require difficult measurement schemes, lack comagnetometry, or are confined to specific species and experimental techniques. It is therefore useful to find a simple approach which offers high sensitivity to *CP* violation and strong robustness against systematic errors without relying on a specific molecular structure.

In this work, we experimentally demonstrate a general method [17] to engineer field-insensitive yet EDM-sensitive clock transitions in paramagnetic species, while simultaneously engineering transitions to sense external fields. The concept of tuning parameters to magic values to suppress some unwanted effect has been successfully applied in a wide range of experiments [21–27], and is, for example, a critical ingredient for the high precision and accuracy of modern atomic clocks [28]. We demonstrate this using the YbOH molecule and show that at particular "magic" values of applied electromagnetic fields, certain transitions exhibit orders-of-magnitude suppression of electric- and magnetic-field sensitivities while maintaining a large (differential) internal effective electric field of $\mathcal{E}_{\mathrm{eff}} \approx 22$ GV/cm [29]. The underlying concept was introduced in Ref. [17]; here we provide its first experimental realization in a heavy polyatomic molecule at the requisite level of quantum control, including all requisite external parameters and their control via experimental "switches" to isolate the desired signal from background noise or systematic errors [30]. The observed suppression of the field sensitivities is measurement statistics limited. This clock transition exhibits simultaneous zero crossings of electric- ($\boldsymbol{\mathcal{E}}$) and magnetic- ($\boldsymbol{\mathcal{B}}$) field sensitivities at a particular electromagnetic-field point (up to measurement precision), though the sensitivities are also considerably reduced over a broad range of electromagnetic-field values. We perform Ramsey measurements and show that coherence is maintained under large external electric- and magnetic-field fluctuations. We further introduce and experimentally demonstrate a new measurement protocol that utilizes both "EDM-clock" (field-insensitive) and "field-sensing" (field-sensitive) transitions to significantly suppress systematic errors in EDM experiments.

This approach does not rely on a particular electronic state (e.g., a $^3\Delta_1$ state), and such magic conditions can be found in a wide range of molecules [17]. Realizing such magic conditions requires (i) sufficient internal complexity to enable complicated mixing among nearby internal states to allow accidental cancellations of field sensitivities and (ii) mixing of opposite-parity states to acquire substantial EDM sensitivity. Since polyatomic molecules generically have suitable opposite-parity states with sufficient internal complexity within approximately 10 MHz of each other [31], these magic conditions can be typically achieved with easily accessible laboratory fields ($\mathcal{E} \lesssim 100$ V/cm.) Diatomics without parity doublets, such as those in $^2\Sigma$ states, generally require nonzero nuclear spin for magic conditions to emerge from their complex hyperfine structure, and large electric fields to mix rotational levels ($\gtrsim$10 kV/cm). Given the generic applicability of the approach, it should be useful for the study of a broad range of new physics observables including eEDM, nuclear Schiff moments (NSMs), nuclear magnetic quadrupole moments (MQMs) [17], as well as for dark-matter searches over many orders of magnitude in mass [32,33]. The basic idea is to identify pairs of states whose electric and magnetic sensitivities can be tuned with external fields to a point where they have vanishing differential Stark and Zeeman shifts, yet retain large differential *CP*-violation sensitivity. The approach can use states that have a small difference in projection of total angular momentum (M_F), making state preparation and readout schemes straightforward. These methods are particularly useful for species with heavy spinful nuclei, which are needed for NSM and MQM searches, and which typically have complex hyperfine structure.

In this work, we shall focus on the eEDM-sensitive molecule ^{174}YbOH [29,31,34]. As discussed in an earlier work [17], apart from experimental parameter differences like electric- and magnetic-field values and laser frequencies, this approach should be very similar in other species, especially polyatomics for which these magic conditions generally appear at comparable field values. The energy shifts induced by the eEDM in a molecule under external fields are governed by the Hamiltonian [35]

$$H = -D\hat{\boldsymbol{n}} \cdot \boldsymbol{\mathcal{E}} - g\mu_B \boldsymbol{S} \cdot \boldsymbol{\mathcal{B}} + d_e \mathcal{E}_{\mathrm{eff}} \hat{\boldsymbol{S}} \cdot \hat{\boldsymbol{n}}. \tag{1}$$

Note that this is a minimal effective Hamiltonian included to highlight the field- and eEDM-dependent contributions relevant for the engineered-transition concept; additional terms (e.g., hyperfine and spin rotation) are included in the full model used for quantitative predictions (see Appendix B). Here, D is the molecular-frame dipole moment, $\hat{\boldsymbol{n}}$ is a unit vector along the molecular (symmetry) axis, g denotes the magnetic g-factor, $\hat{\boldsymbol{S}}$ is the unit vector along the electron spin, d_e is the electron EDM, and $\mathcal{E}_{\mathrm{eff}}$ is the internal effective field experienced by the electron.

The relative orientation of $\hat{\boldsymbol{S}}$ and $\hat{\boldsymbol{n}}$, defined as $P \equiv \langle \hat{\boldsymbol{S}} \cdot \hat{\boldsymbol{n}} \rangle$, serves as a quantum-state-specific measure of the eEDM sensitivity. In this manuscript, we refer to $\mathcal{E}_{\text{eff}} P$ as the "eEDM sensitivity" since each state may have a different value of P.

II. RESULTS

A schematic representation of the experiment is shown in Fig. 1(a). YbOH molecules are produced via laser ablation of pressed targets in a 4-K cryogenic buffer-gas cell and extracted as a cryogenic buffer-gas beam (CBGB) with forward velocity $v \approx 200$ m/s. After state preparation via 567-nm optical pumping into the "science state" $|\tilde{X}(010), N'' = 1, p = +\rangle$ manifold, a Ramsey measurement on the transition of interest, denoted by the states $|0\rangle$ and $|1\rangle$, is performed via two-photon Raman pulses in a region of controllable electric and magnetic fields generated by indium-tin-oxide- (ITO) coated glass plates and wire coils, respectively. Here, N denotes the molecular angular momentum not including spin, p is the parity, and (010) means that the molecule has one quanta of bending vibration. This bending motion leads to parity doubling, making this state useful as the science state for EDM measurements [31]. $\tilde{X}$ denotes the ground electronic state. There are three additional few-meter-scale pairs of coils, which null ambient magnetic fields to the mG level. Zeeman spectroscopy confirms that field uncertainties are approximately 1 mG and therefore have negligible impact on our extraction of the field sensitivities.

YbOH molecules in the beam experience two Ramsey pulses. The first $\pi/2$-pulse creates a superposition $|\psi\rangle \propto |0\rangle + |1\rangle$. For conceptual clarity, we describe an ideal model with a perfect $\pi/2$-pulse, though our analysis includes imperfections in the pulses. The state then evolves into $|\psi\rangle \propto |0\rangle + e^{i\varphi}|1\rangle$ in the applied fields for a time $\tau \approx 25$ μs over a distance of approximately 5 mm. Here the phase φ contains all physical phase accumulation, including the Stark and Zeeman shifts, the eEDM, and more [30]. The second $\pi/2$-pulse projects φ onto the populations in $|0\rangle$ and $|1\rangle$, yielding $|\psi\rangle \propto \cos(\varphi/2)|0\rangle + i\sin(\varphi/2)|1\rangle$. Finally, φ is read out by laser-induced fluorescence to form an asymmetry signal $\mathcal{A} = (N_0 - N_1)/(N_0 + N_1)$ and suppress unwanted effects arising from beam yield fluctuations both within a single pulse and between different pulses. Both populations of states $|0\rangle$ and $|1\rangle$ are measured via fast frequency switching [36] (see Appendix A 2). A representative Ramsey fringe is shown in Fig. 1(b). Note that imperfect optical pumping leaves populations in states close in energy to $|0\rangle$ and $|1\rangle$, and their fluorescence adds background ($\mathcal{A}_0$) and reduces the Ramsey contrast ($\mathcal{C}$).

Here we focus on a specific set of transitions in ^{174}YbOH that fall into two classes: an EDM-clock transition, whose sensitivities to both electric and magnetic fields are tuned to be simultaneously suppressed while maintaining high eEDM sensitivity, and a field-sensing transition, which

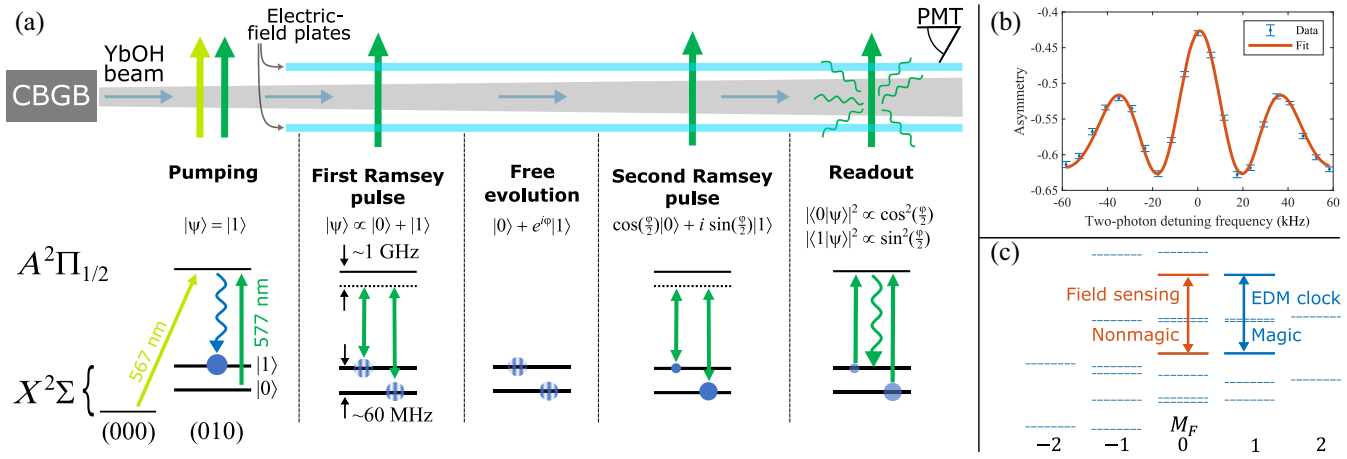

FIG. 1. (a) A schematic representation of the experiment. A beam of YbOH molecules is directed through a series of lasers. The first lasers optically pump from the ground nonvibrating (000) state to populate the $|1\rangle$ level in the (010) bending mode science state. Next, a two-photon pulse creates a coherent superposition of $|0\rangle$ and $|1\rangle$. During spin precession, a phase φ is accumulated. A second two-photon pulse then maps the relative phase onto populations of $|0\rangle$ and $|1\rangle$. (The second Ramsey pulse is derived from the same laser but delivered downstream along a separate beam path.) Finally, state populations are determined by state-selective laser-induced fluorescence detected on a photomultiplier tube (PMT). (b) An example Ramsey fringe taken with $\mathcal{E} = 10.93$ V/cm and $\mathcal{B} = 0.30$ G as a function of the two-photon frequency. Blue points indicate measured data, and the red curve is a fit to $\mathcal{A}(\delta)$, whose full expression is given in Appendix A 2. Error bars denote 1σ standard deviations of repeated asymmetry measurements taken under the same experimental conditions. (c) Level diagrams of the $N'' = 1$, $\tilde{X}(010)$ state in ^{174}YbOH at $\mathcal{E} = 39.60$ V/cm and $\mathcal{B} = 12.15$ G, highlighting the EDM-clock transition that suppresses both electric- and magnetic-field sensitivities and nearby field-sensing transition used for field sensing.

retains high sensitivity to electric and magnetic fields. These two classes of transitions are employed in different experimental contexts throughout this work. Figure 1(c) shows an EDM-clock transition and a field-sensing transition operated at the same electric and magnetic fields to demonstrate the switching protocol. The field-sensing transition used in the noise-robustness measurements of Fig. 3 is a different field-sensing transition chosen at different field values to enhance sensitivity to applied field fluctuations. In addition, the EDM-clock transition used for the Ramsey fringe demonstration in Fig. 1(b), which is operated at different electric and magnetic fields from Fig. 1(c), is chosen as an example with good signal-to-noise ratio and is discussed in detail in Appendix C. This is an example of the other engineered transitions with different sensitivities to fields and *CP*-violation effects [17]. We conduct two-photon spectroscopy to locate the line position of the EDM-clock transitions at various electric and magnetic fields and perform Ramsey measurements to measure their Stark and Zeeman shift to extract the field sensitivities. A detailed description of the extraction procedure, together with the associated uncertainty propagation, is provided in Appendix A 3.

To quantify the sensitivity of a particular transition between two states $|0\rangle$ and $|1\rangle$ to $\boldsymbol{\mathcal{B}}$, $\boldsymbol{\mathcal{E}}$, and d_e, we define the following differential quantities: the differential effective magnetic moment $\Delta\mu_{\mathrm{eff}} \equiv \mu_{\mathrm{eff},0} - \mu_{\mathrm{eff},1}$ in MHz/G, the differential effective dipole moment $\Delta d_{\mathrm{eff}} \equiv d_{\mathrm{eff},0} - d_{\mathrm{eff},1}$ in MHz/(V/cm), and the differential eEDM sensitivities $\Delta P \equiv (P_0 - P_1)$. For the $\tilde{X}(010)$ state in YbOH, the maximum differential eEDM sensitivity obtainable in the limit of full mixing of the parity doublets (i.e., at electric fields that are large enough to fully mix parity doublets) is given by $\Delta P_{\mathrm{max}} = |P_{N''=1,M_F=2,M_N\ell=1} - P_{N''=1,M_F=2,M_N\ell=-1}| = 1$, where $M_N\ell$ indicates molecular orientation in the lab-frame axis. This is the EDM sensitivity conventionally considered, as many EDM experiments operate at sufficiently high electric fields, and is therefore used as a reference in this manuscript. Note, however, that at the "intermediate" electric-field regime, there are also local sensitivity maxima, which can result in ΔP exceeding 1, as observed elsewhere [20,37]. Note also that the angular momentum coupling in $|\tilde{X}(010), N'' = 1\rangle$ results in the molecular polarization on the lab-frame $\hat{\boldsymbol{Z}}$ axis of $\langle \hat{\boldsymbol{n}} \cdot \hat{\boldsymbol{Z}} \rangle = \{(M_N\ell)/[N''(N''+1)]\}$, where ΔP_{max} is smaller by a factor of 2 than in a $^3\Delta_1$ state. Without employing engineered EDM-clock transitions, typical transitions have electromagnetic sensitivities given by the molecular dipole moment $D = 2.16$ Debye and Bohr magneton μ_B [38]. These parameters yield sensitivities of $\Delta d_{\mathrm{typ}} \sim 1$ MHz/(V/cm) and $\Delta\mu_{\mathrm{typ}} \sim 1.4$ MHz/G.

The observed field sensitivities of the EDM-clock transition exhibit zero crossings and are consistent with the predictions using the molecular parameters from previous optical spectroscopy to within the expected uncertainties [38]. These zero crossings are summarized in Fig. 2. This indicates that EDM-clock transitions can be located with only moderate uncertainty on spectroscopic parameters. The observed field sensitivities are $\Delta d_{\mathrm{eff}} = (-0.0009 \pm 0.0006)$ MHz/(V/cm) and $\Delta\mu_{\mathrm{eff}} = (-0.0004 \pm 0.0055)$ MHz/G, or $|\Delta d_{\mathrm{eff}}| < 0.0015$ MHz/(V/cm) and $|\Delta\mu_{\mathrm{eff}}| < 0.006$ MHz/G. This corresponds to a suppression in electric- and magnetic-field sensitivities by at least a factor of 710 and 230 compared to Δd_{typ} and $\Delta\mu_{\mathrm{typ}}$, respectively. Note that the sensitivities are predicted to be even lower, so these limits correspond to our ability to measure them directly.

At the same time, the EDM-clock transition maintains a large internal effective electric field of $\mathcal{E}_{\mathrm{eff}}\Delta P \approx 22$ GV/cm, or $\Delta P/\Delta P_{\mathrm{max}} \gtrsim 93\%$. This indicates that one can suppress the electromagnetic-field sensitivities by orders of magnitude while maintaining high eEDM sensitivity. It is worth mentioning that our upper limit of magnetic sensitivity in the magic condition is on the same order of the $^3\Delta_1$ state in ThO [36] and HfF^+ [39].

A key component of the Ramsey measurement is coherence. Suppressing decoherence enables longer coherence times and thus enhances the statistical sensitivity to the eEDM. To demonstrate robustness against decoherence from electric and magnetic fields, we measure the contrast of a Ramsey fringe with applied field noise and compare the EDM-clock transition to a field-sensing transition with large field sensitivities. Note that the field-sensing transition discussed here is different from the field-sensing transition shown in Fig. 1(c) and is chosen for its higher field sensitivities. Applied field amplitudes are varied shot to shot with a uniform distribution. Ramsey contrast $\mathcal{C}$ is extracted by the measurement of the asymmetry difference $\mathcal{A}(\delta = 0) - \mathcal{A}[\delta = (\pi/\tau)] \propto \mathcal{C}$. The contrast of field-sensing transitions decays rapidly with field noise amplitudes of $\lesssim$0.1 V/cm and $\lesssim$0.02 G, whereas the EDM-clock transitions tolerate noise amplitudes of $\lesssim$10 V/cm and $\lesssim$1 G as shown in Fig. 3 and consistent with predictions (see Appendix D). Note that the contrast decay observed here reflects how far the suppression remains robust as one moves away from the magic point. This measurement does not directly determine the local first-order Stark or Zeeman sensitivity at the magic point itself, which remains limited by our ability to resolve small frequency shifts.

We can model the contrast decay under applied field noise by mapping field fluctuations to an effective distribution of two-photon detunings using the measured first derivative of the field sensitivities of the EDM-clock transitions. The measured contrast corresponds to an ensemble average of the Ramsey fringe over this detuning distribution. To provide a simple quantitative interpretation of the contrast roll-off in Fig. 3, we model the clock-transition frequency shift (δf) near the magic point in terms of electric- and magnetic-field shifts from the magic point ($\delta E, \delta B$),

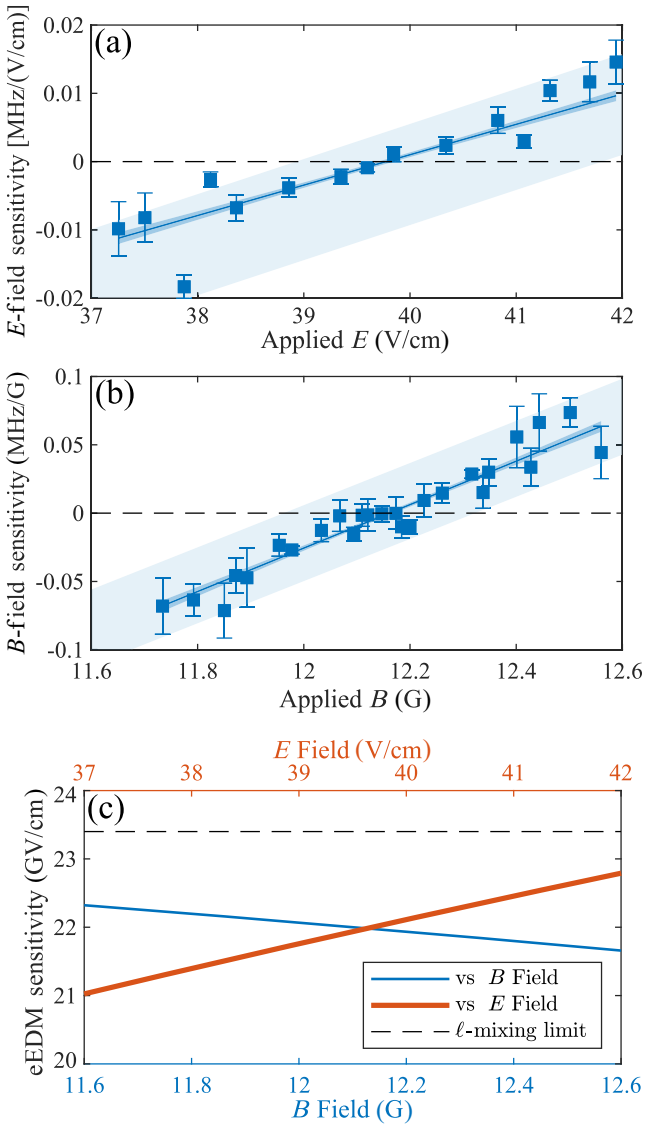

FIG. 2. (a) Measured electric-field sensitivity, (b) measured magnetic-field sensitivity, and (c) calculated eEDM sensitivity of the EDM-clock transition as functions of the applied electric and magnetic fields. (a),(b) Field sensitivities are expressed as the effective electric dipole moment and effective magnetic dipole moment. Blue square points represent measurements, blue lines are linear fits, dark shaded regions indicate the fit uncertainties, and light shaded regions show the original theory uncertainty based on earlier spectroscopic measurements [17]. Error bars denote 1σ uncertainties in the extracted field sensitivities obtained by the standard error-propagation procedure described in Appendix. A 3. The applied magnetic field in (a) is 12.15 G, and the applied electric field in (b) is 39.60 V/cm. Linear fits yield $(\partial\Delta\mu_{\rm eff}/\partial\mathcal{B}) = (1.6 \pm 0.1) \times 10^{-1}$ MHz/G^2 and $(\partial\Delta d_{\rm eff}/\partial\mathcal{E}) = (4.4 \pm 0.3) \times 10^{-3}$ MHz/(V/cm)^2, demonstrating that high suppression of $\Delta d_{\rm eff}$ and $\Delta\mu_{\rm eff}$ is maintained over a range of a few V/cm and approximately 1 G, respectively. (c) The predicted eEDM sensitivity based on molecular parameters provided in Appendix B is expressed in terms of $\mathcal{E}_{\rm eff}\Delta P$ (GV/cm). The solid blue line is at 39.6 V/cm, and the red line is at 12.15 G. The dashed black lines indicate the maximum eEDM sensitivity attainable in the limit of full mixing of the ℓ parity doublets.

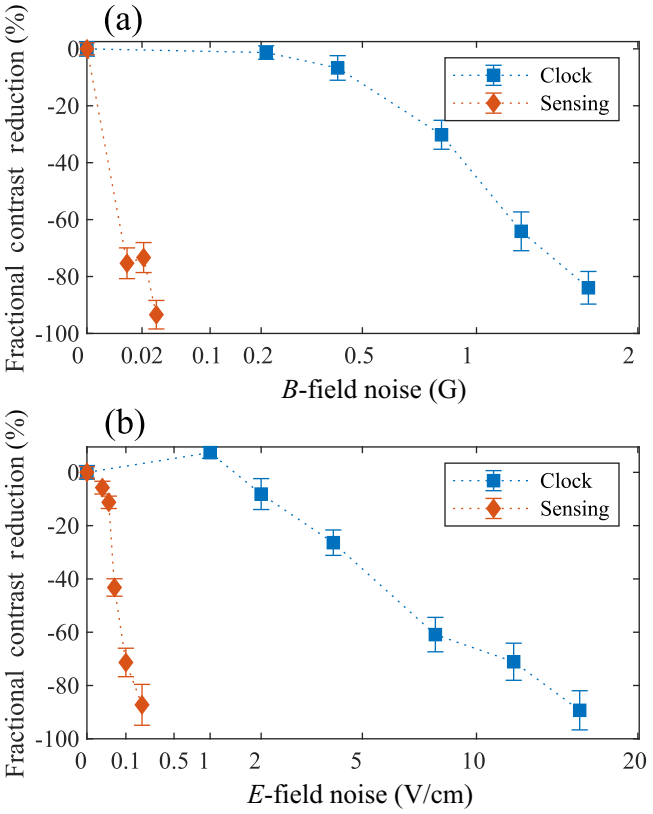

FIG. 3. Reduction in Ramsey fringe contrast as a function of the electric- and magnetic-field noise amplitude. The noise has uniform distribution with amplitude defined as the difference between the minimum and maximum values. The x-axis scale is nonlinear to more clearly show the behavior at low noise values. Data in (a) were taken with zero applied electric-field noise, and in (b) with zero applied magnetic-field noise. The applied field noise distributions are centered at $\mathcal{E} = 39.60$ V/cm and $\mathcal{B} = 12.15$ G for the EDM-clock ("Clock") transition, and $\mathcal{E} = 20.00$ V/cm and $\mathcal{B} = 0.30$ G for the field-sensing ("Sensing") transition. Error bars denote 1σ uncertainties obtained by standard error propagation of the asymmetry difference, where the uncertainty of each asymmetry is taken as the 1σ standard deviation of repeated asymmetry measurements under the same experimental conditions. The field sensitivities of the field-sensing transition around these fields are $\Delta d_{\rm eff} = (0.120 \pm 0.001)$ MHz/(V/cm) $\sim 0.1\Delta d_{\rm typ}$ and $\Delta\mu_{\rm eff} = (0.952 \pm 0.008)$ MHz/G $\sim \Delta\mu_{\rm typ}$. The applied field noise distribution is discretized due to the finite resolution of the current and voltage supply for the magnetic coil and electric-field plate, respectively. The applied fields sample 20–1300 discrete values for the EDM-clock transition and 2–25 discrete values for the field-sensing transition.

$$\delta f \simeq \frac{1}{2}\left(\frac{\partial\Delta\mu_{\rm eff}}{\partial B}\right)\delta B^2 + \frac{1}{2}\left(\frac{\partial\Delta d_{\rm eff}}{\partial E}\right)\delta E^2, \qquad (2)$$

using the experimentally measured curvatures $(\partial\Delta\mu_{\rm eff}/\partial B)$ and $(\partial\Delta d_{\rm eff}/\partial E)$. The accumulated phase is $\delta\phi \sim 2\pi\delta f T$. Assuming uniform noise distributions $\delta B \sim$ Uniform$[-B_n, B_n]$ and $\delta E \sim$ Uniform$[-E_n, E_n]$, one finds

$\mathrm{Var}(\delta B^2) = (4/45)B_n^4$ and $\mathrm{Var}(\delta E^2) = (4/45)E_n^4$. This yields frequency fluctuations

$$\sigma_{f,B} \simeq \frac{1}{\sqrt{45}}\left|\frac{\partial \Delta\mu_{\mathrm{eff}}}{\partial B}\right| B_n^2, \qquad \sigma_{f,E} \simeq \frac{1}{\sqrt{45}}\left|\frac{\partial \Delta d_{\mathrm{eff}}}{\partial E}\right| E_n^2. \tag{3}$$

A noticeable contrast reduction begins when $\sigma_f \sim (2\pi T)^{-1}$, consistent with the qualitative roll-off observed in Fig. 3. For example, taking $T \simeq 25$ μs gives $(2\pi T)^{-1} \simeq 6.4$ kHz, which corresponds [using $(\partial\Delta\mu_{\mathrm{eff}}/\partial B) = 1.6 \times 10^{-1}$ MHz/G^2 and $(\partial\Delta d_{\mathrm{eff}}/\partial E) = 4.4 \times 10^{-3}$ MHz/(V/cm)^2] to the onset of contrast roll-off at $B_n \simeq 0.52$ G or $E_n \simeq 3.1$V/cm.

For the field-sensing transition, the dominant frequency shift is linear in the applied fields,

$$\delta f \simeq \Delta\mu_{\mathrm{eff}}\delta B + \Delta d_{\mathrm{eff}}\delta E. \tag{4}$$

Since $\mathrm{Var}(\delta B) = B_n^2/3$ and $\mathrm{Var}(\delta E) = E_n^2/3$, the frequency fluctuation is

$$\sigma_{f,B} \simeq \Delta\mu_{\mathrm{eff}}\frac{B_n}{\sqrt{3}}, \qquad \sigma_{f,E} \simeq \Delta d_{\mathrm{eff}}\frac{E_n}{\sqrt{3}}. \tag{5}$$

Using experimentally measured field sensitivities $\Delta d_{\mathrm{eff}} = (0.120 \pm 0.001)$ MHz/(V/cm) and $\Delta\mu_{\mathrm{eff}} = (0.952 \pm 0.008)$ MHz/G for field-sensing transitions here gives $B_n \simeq 12$ mG or $E_n \simeq 92$ mV/cm. Using the measured sensitivities and the applied noise amplitudes, this simple model reproduces the observed qualitative trends and provides an order-of-magnitude estimate for the noise level at which contrast begins to roll off.

Our approach also provides the tools to sense and correct field imperfections which could give rise to eEDM-mimicking systematic errors—a primary obstacle in experiments. In particular, background "nonreversing" electric and magnetic fields ($\mathcal{E}_{\mathrm{NR}}$, $\mathcal{B}_{\mathrm{NR}}$), which do not change when the applied fields are purposefully reversed, are a common concern. Here, we show that alternating between EDM-clock-transition and field-sensing-transition measurements can sense the electric and magnetic environment directly. Since the approach here uses the same rotational state in the molecule and the same lasers are used for the measurement, this approach can also be used to directly sense higher-order effects which rely on the combination of multiple errors, such as those observed with ThO [30]. Since many nearby field-sensing transitions exist within the same electronic and vibrational state, alternating between EDM-clock-transition and field-sensing transition is straightforward; we simply adjust the two-photon frequency detuning. In our case, we change the frequency of the acousto-optic modulator which generates the two-photon detuning approximately by 400 kHz. Note that under our experimental conditions, the two-photon linewidth is approximately 200 kHz. The approximately 400-kHz frequency shift used to address the field-sensing transition is therefore sufficient to avoid significant spectral overlap with the EDM-clock transition at the level relevant for the present demonstration; alternative field-sensing transitions with larger spectral separations are also available if needed to avoid any potential complications from proximity in frequency. Furthermore, because the transition can be connected via linearly polarized light in the presence of a magnetic field, one can reverse the eEDM shift by reversing only the electric or magnetic field, without changing the laser polarization. Since the laser is polarized along the electric-field direction, the laser does not need to be sent through the electric-field plates, offering further technical advantages [30].

To isolate the eEDM shift from other shifts, we measure the transition frequency f under all combinations of three binary "switches": the electric-field up and down switch ($\hat{\mathcal{E}}$), the magnetic field up and down switch ($\hat{\mathcal{B}}$), and the EDM-clock and field-sensing (magic and nonmagic) switch ($\hat{\mathcal{M}}$). The EDM-clock transition and field-sensing transition employed here are shown in Fig. 1(c). We then take linear combinations of these eight frequencies to form "switch channels" denoted by f^s so that each channel singles out effects correlated with the listed switches s [30]. For instance, $f^{\mathcal{EB}}$ singles out the effects correlated with both $\hat{\mathcal{E}}$ and $\hat{\mathcal{B}}$ switches but not the $\hat{\mathcal{M}}$ switch and contains both the genuine eEDM signal and potential eEDM-mimicking systematic effects. On the other hand, the switch channels $f^{\mathcal{ME}}$ and $f^{\mathcal{MB}}$ serve as sensitive probes of $\mathcal{E}_{\mathrm{NR}}$ and $\mathcal{B}_{\mathrm{NR}}$ with measured slopes $f^{\mathcal{ME}}/\mathcal{E}_{\mathrm{NR}} = (17.2 \pm 1.5)$ kHz/(V/cm) and $f^{\mathcal{MB}}/\mathcal{B}_{\mathrm{NR}} = (-65.6 \pm 6.4)$ kHz/G, respectively (Fig. 4). The uncertainties are computed from a statistical ensemble of 120 molecular pulses per data point. This enables highly sensitive measurements of the electromagnetic fields directly, using the same science state, same lasers, same preparation and readout scheme, etc., thereby providing a very robust and easy-to-implement approach to field sensing and comagnetometry—a feature challenging to realize with other approaches. Note that these field-sensing transitions are measured independently and used exclusively for systematic studies: to monitor electric and magnetic fields, to search for correlations that could generate EDM-mimicking effects, and to correct these effects if necessary. The cadence with which the measurements on the field-sensing transitions are interleaved with the EDM measurements is determined by the characteristic timescale over which relevant systematic effects are expected to vary. Slowly drifting field imperfections may require only occasional field-sensing measurements, while more rapidly varying effects need to be probed more frequently as needed, without compromising the intrinsic field insensitivity of the EDM channel.

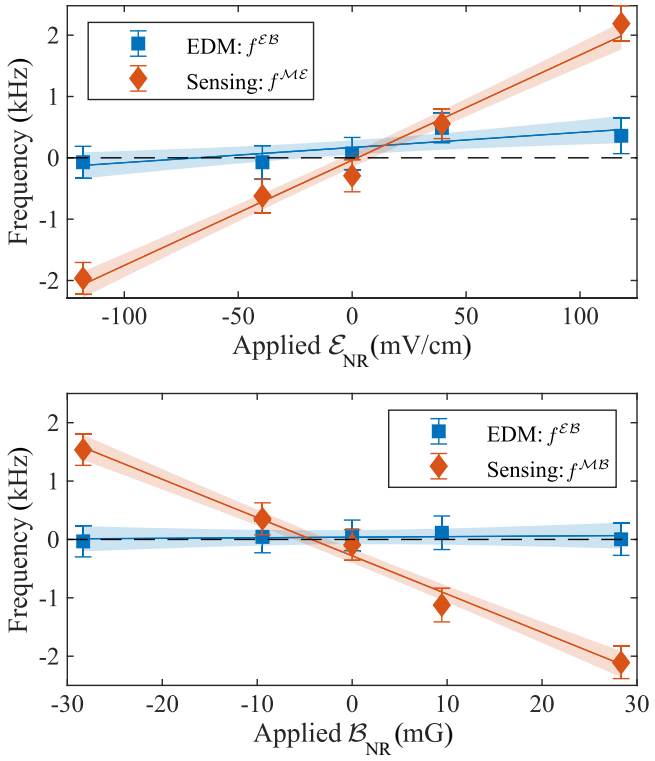

FIG. 4. $f^{\mathcal{ME}}$, $f^{\mathcal{MB}}$, and $f^{\mathcal{EB}}$ measured at various applied $\mathcal{E}_{\mathrm{NR}}$ and $\mathcal{B}_{\mathrm{NR}}$. Data in (a) were taken at applied $\mathcal{B}_{\mathrm{NR}} = 0$ G and in (b) at applied $\mathcal{E}_{\mathrm{NR}} = 0$ V/cm. Blue (square) and orange (diamond) points represent measurements, while the corresponding blue and orange solid lines are linear fits to the data. Error bars denote 1σ uncertainties in the extracted frequency shifts obtained by the standard error-propagation procedure described in Appendix. A 3. The shaded regions indicate the uncertainty of the fit. The fit results for $f^{\mathcal{EB}}/\mathcal{E}_{\mathrm{NR}}$ and $f^{\mathcal{EB}}/\mathcal{B}_{\mathrm{NR}}$ are (2.5 ± 1.5) kHz/(V/cm) and (1.0 ± 6.4) kHz/G, which are smaller than that of $f^{\mathcal{ME}}/\mathcal{E}_{\mathrm{NR}}$ and $f^{\mathcal{MB}}/\mathcal{B}_{\mathrm{NR}}$, respectively. All the data in this figure are taken at $\mathcal{E} = 10.93$ V/cm and $\mathcal{B} = 0.30$ G. "EDM" and "Sensing" refer to EDM-clock and field-sensing transition, respectively.

These measured fields can then be used to shim out field imperfections, or calculate and subtract systematic errors arising from them, analogous to the approach utilized in HfF^+ [40]. Additionally, our scheme works for higher-order effects like field imperfections coupled to laser effects [30], since the same lasers are used in the $\hat{\mathcal{M}}$ switch. There are also added benefits of high sensitivity to both electric and magnetic fields, and the ability to directly measure them without relying on auxiliary measurements, in contrast to the scheme in ThO [30,41]. For example, offset fields can be deliberately applied to shim out nonreversing fields by minimizing shifts in $f^{\mathcal{ME}}$ and $f^{\mathcal{MB}}$. Additionally, the false eEDM arising from a simultaneous nonreversing electric and magnetic field [30] $d_e^{\mathrm{false}} \propto \mathcal{E}_{\mathrm{NR}}\mathcal{B}_{\mathrm{NR}}$ can be determined from the $f^{\mathcal{MB}}$ and $f^{\mathcal{ME}}$ channels since $\mathcal{E}_{\mathrm{NR}}\mathcal{B}_{\mathrm{NR}} \propto f^{\mathcal{MB}} f^{\mathcal{ME}}$. This shows that the switching between EDM-clock transitions and field-sensing transitions serve as a robust protocol against systematic effects induced by uncontrolled electromagnetic fields. Other channels such as $f^{\mathcal{E}}, f^{\mathcal{B}}, f^{\mathcal{MEB}}$ also provide additional cross-checks of the eEDM signal and stray fields. Note that while $\mathcal{E}_{\mathrm{NR}}$ and $\mathcal{B}_{\mathrm{NR}}$ are important cases of systematic errors that we examine in detail in this work, other systematic errors can be introduced by additional imperfections, such as field gradients and transverse fields arising from misalignment between electric field, magnetic field, and laser polarization axis, all of which require careful consideration and measurement. Importantly, a range of EDM-clock transitions and field-sensing transitions with different sensitivities to different imperfections can be selected to diagnose and mitigate these systematic errors [17], in addition to auxiliary measurements and other standard approaches [30].

III. DISCUSSION AND CONCLUSIONS

In summary, we present the first experimental demonstration of engineered clock transitions that simultaneously suppress the sensitivities to electric and magnetic fields by orders of magnitude, enable sensing of the electromagnetic environment, and offer high sensitivity to a wide range of new physics, including fundamental symmetry violations and dark matter. The protocol is versatile and well suited for a wide range of species, including those with large angular momentum commonly encountered in nuclear CP-violation searches, such as a nuclear MQM search [17,31,42] and many more [43–45].

Employing our protocol in YbOH offers two key advantages. First, laser cooling and slowing can potentially increase both the usable interaction time and the detected molecule number. Direct laser cooling of YbOH has been demonstrated [46], and related work in YbF has realized ultracold, substantially brighter molecular beams and outlines pathways for beam-based precision measurements [47–49] which could reach $<10^{-31}$ e cm sensitivity. Such methods are applicable to YbOH, offering potential eEDM constraint comparable to YbF assuming the same experimental conditions, but with the added benefits of field-insensitive measurements schemes and tunable electromagnetic moments available at much lower electric fields by roughly 3 orders of magnitude, like those demonstrated here, thanks to the parity doublets. This reduction of required electric fields for field insensitivity and robustness against systematic errors is important as statistical sensitivity improves, and will be useful when implementing new approaches such as optical dipole trapping for even further sensitivity improvements. Second, YbOH is a compelling platform for the study of nuclear symmetry violation, where these EDM-clock transitions provide relatively straightforward measurement protocols even in species with very complex hyperfine structure [17]. Our current

efforts with this apparatus are focused on searching for the MQM in ^{173}YbOH using this EDM-clock approach.

Similar magnetically insensitive transitions have been demonstrated in rare-earth–ion-doped crystals [50] and our scheme could be adopted for solid-state dark-matter and *CP*-violation searches [51]. The tunability of field sensitivities via application of external fields, combined with ultracold assembly or electromagnetic control techniques (electric and magnetic guiding, optoelectrical and ion trapping) could extend the protocol to non-laser-coolable species in symmetry-violation searches [52–54]. Looking forward, these EDM-clock transitions could be also combined with quantum-enhanced protocols to further boost sensitivity to *CP*-violating signals while retaining suppression of field sensitivities, and the present work establishes the transition engineering and control tools needed for such future extensions [55]. Beyond these applications in fundamental nuclear and particle physics, engineered clock transitions in polarized molecules naturally offer long interaction times with long-range dipole-dipole interactions, and thus could benefit molecular quantum simulation and computation [1,54,56,57] and ultracold chemistry [2]. Our demonstration, together with these prospects, suggests that engineered clock transitions can suppress decoherence and systematic errors across diverse platforms, holding promise for molecular quantum science and fundamental physics.

ACKNOWLEDGMENTS

We thank John M. Doyle, Xing Fan, Zack Lasner, Kon Leung, Amar Vutha, Chandler Conn, and Phelan Yu for feedback on the manuscript. This work was supported by the Heising-Simons Foundation (Grant No. 2019-1193 and No. 2022-3361), the Rose Hills Foundation, and an NSF CAREER Award (Award No. PHY-1847550). Y. T. was supported by an IQIM Eddleman Fellowship and the Masason Foundation. H. D. R. was supported by a Fulbright Scholarship. C. Z. was supported by the Caltech David and Ellen Lee Postdoctoral Fellowship.

Y. T. developed the concept and, with N. R. H., conceived the project. Y. T., H. D. R., Y. Z., and C. Z. designed and built the experiment. Y. T. and H. D. R. performed the measurements. Y. T. and N. R. H. analyzed the data. Y. T., H. D. R., C. Z., and A. J. performed spectroscopy to predict and identify molecular structure. Y. T., A. J., and C. Z. performed early investigations into the clock-based approach. Y. T. and N. R. H. wrote the manuscript. N. R. H. supervised the project.

The authors declare no competing interests.

DATA AVAILABILITY

The data that support the findings of this article are openly available [58].

APPENDIX A: EXPERIMENT DETAILS

1. Experimental apparatus

In the experiment, YbOH molecules are produced by laser ablation of pressed powder targets at an approximately 1-Hz repetition rate and subsequently thermalized by collisions with approximately 4-K He buffer gas atoms in a cryogenic buffer-gas cell. By resonantly driving the $^1S_0 \rightarrow {}^3P_1$ transition of ^{174}Yb, the ^{174}YbOH yield is increased by around an order of magnitude [59]. YbOH is extracted through the cell aperture as a rotationally and translationally cold beam [60,61]. The YbOH beam travels at approximately 200 m/s through a room-temperature chamber where YbOH is optically pumped from $|\tilde{X}(000), N'' = 0, p = +\rangle$ to $|\tilde{X}(010), N'' = 1, p = +\rangle$ through the $|\tilde{A}(010), p = -\rangle$ excited state using a laser at 567 nm [62]. There are no applied electric or magnetic fields in this region, so the parity selection rules hold.

The YbOH molecules then enter the "science chamber" located approximately 112 cm downstream from the cell where the Ramsey measurement and laser-induced fluorescence (LIF) detection are performed. Inside the science chamber, two ITO-coated glass plates separated by one inch apply a uniform electric field in the vertical direction, which defines the lab $\hat{\boldsymbol{Z}}$ axis. Since the electric field applied in this work remains below the regime of full parity-doublet mixing [17,38], a substantial fraction of the population in $|N'' = 1, p = +\rangle$ is transferred to the science states used in this work, such as $|0\rangle$ and $|1\rangle$, under the electric field in the science chamber. This allows us to optically pump from $|\tilde{X}(000), N'' = 0, p = +\rangle$ to $|\tilde{X}(010), N'' = 1, p = +\rangle$ before the YbOH beam enters the electric-field region in the science chamber, as can be seen from Fig. 1(a). This configuration is advantageous because it significantly reduces scattered light from the high-power optical pumping lasers reaching the final detector, thereby lowering the background signal.

In the science chamber, YbOH molecules are illuminated with multiple lasers at 577 nm to perform Ramsey spin precession measurements. Note that the lasers are always on, and the motion of the molecules through the fixed laser beams results in them experiencing temporal pulses. Here the transitions of interest consist of $|0\rangle$ and $|1\rangle$ in $|\tilde{X}(010), N'' = 1, p = +\rangle$, roughly separated by approximately 60 MHz. To be clear, depending on the measurement, these may be different states. The states used for the $\hat{\mathcal{M}}$ switch (changing between the EDM-clock transition and field-sensing transition) demonstration are shown in Fig. 1 in the main text. The first laser optically pumps from $|0\rangle$ to $|1\rangle$ through a $|\tilde{A}(010), p = -\rangle$ excited state with $\hat{Z}$ polarization. Next, the YbOH beam sees two Ramsey pulses. Note that we describe an ideal model with a perfect $\pi/2$-pulse for conceptual clarity, though our quantitative analysis uses a fit function that incorporates measured deviations from a perfect $\pi/2$-pulse. The first is a $\pi/2$-pulse

with a two-photon laser phase θ to create a superposition $|\psi(0)\rangle \propto |0\rangle + e^{i\theta}|1\rangle$. This state then evolves into $|\psi(\tau)\rangle \propto |0\rangle + e^{i(\varphi+\theta)}|1\rangle$ under the applied fields for a time $\tau \approx 25\ \mu s$ over a distance of approximately 5 mm with approximately 200-m/s molecular-beam forward velocity. Note that this distance is between the center of two Ramsey pulse lasers. The laser beam for the Ramsey pulses is elliptical, with the major axis oriented vertically. The measured second moment width of the Gaussian fit along the horizontal (molecular beam) axis is 2.88 mm. The phase accumulation occurs during the Ramsey pulse as well, so the Ramsey fringe period is $\tau \sim \tau_{\text{free}} + T$. The second Ramsey pulse projects the phase φ onto the populations in $|0\rangle$ and $|1\rangle$. Note that the second Ramsey pulse is derived from the same laser but delivered downstream along a separate beam path, and therefore has a constant two-photon laser phase offset $\delta\theta$ from the first pulse, up to the fluctuation of the path length difference. The phase φ contains all physical phase accumulation, including the Stark and Zeeman shifts, the eEDM, and more [30]. The Ramsey pulses are realized via two-photon Raman transitions with the driving laser detuned by approximately 0.5 GHz from the optical resonance between $|\tilde{X}(010)\rangle$ and $|\tilde{A}(010)\rangle$. (For some field-sensing transitions, the detuning was set to 1 GHz.) A double-passed acousto-optic modulator (AOM) generates a single sideband with the carrier, and their beats address the EDM-clock transitions and field-sensing transitions of interest. Note that the Ramsey pulse beams are frequency shifted using AOMs in a double-pass configuration, such that the resulting optical frequency shift is twice the applied rf frequency; unless otherwise stated, all frequency shifts quoted in this work refer to the corresponding optical (two-photon) frequencies. Finally, the last laser drives from $|0\rangle$ or $|1\rangle$ to $|\tilde{A}(010), p = -\rangle$, and the resulting LIF from decays to $|\tilde{X}(010), p = +\rangle$ at 577 nm is collected to give state populations from which φ is inferred. All laser frequencies are locked to a wave meter.

2. Measurement of asymmetry

When we calculate the asymmetry, we form the background-subtracted asymmetry

$$\mathcal{A} = \frac{(M_0 - B_0) - (M_1 - B_1)}{(M_0 - B_0) + (M_1 - B_1)} = \frac{N_0 - N_1}{N_0 + N_1}, \quad \text{(A1)}$$

where $M_{0,1}$ are the raw detected photon counts in the $|0\rangle$ and $|1\rangle$ detection channels, $B_{0,1}$ are the laser-scatter backgrounds measured approximately 30 ms after the ablation where there is no molecular signal, and $N_i \equiv M_i - B_i$ are the background-subtracted signals. Assuming the photon shot noise,

$$\text{Var}(N_i) \sim (N_i + B_i) + B_i = N_i + 2B_i. \quad \text{(A2)}$$

Propagating uncertainties for $\mathcal{A} = (N_0 - N_1)/(N_0 + N_1)$ yields

$$\begin{aligned}\Delta\mathcal{A}^2 &= \left(\frac{\partial\mathcal{A}}{\partial N_0}\right)^2 \text{Var}(N_0) + \left(\frac{\partial\mathcal{A}}{\partial N_1}\right)^2 \text{Var}(N_1) \\ &= \left(\frac{2N_1}{(N_0+N_1)^2}\right)^2 \text{Var}(N_0) \\ &\quad + \left(\frac{2N_0}{(N_0+N_1)^2}\right)^2 \text{Var}(N_1). \end{aligned} \quad \text{(A3)}$$

Using representative values $N_0 \simeq 4500$, $N_1 \simeq 2500$, and $B_0 \simeq B_1 \simeq 6000$ photons, Eq. (A2) gives $\text{Var}(N_0) = N_0 + 2B_0 = 16500$ and $\text{Var}(N_1) = N_1 + 2B_1 = 14500$. Substituting into Eq. (A3) yields $\Delta\mathcal{A} \simeq 0.026$ per shot.

To normalize against molecular yield variations from pulse to pulse and the nonuniform temporal shape of the molecular pulse within each pulse, we employ fast switching [36] of the detection laser frequency to alternate the LIF detection between $|0\rangle$ and $|1\rangle$ at 50 kHz. With this approach, we can construct the asymmetry $\mathcal{A} = (N_0 - N_1)/(N_0 + N_1)$ within a single ablation pulse, which significantly reduces unwanted effects arising from pulse-to-pulse fluctuations and allows us to approach shot-noise-limited measurements. The observed $N_0 \sim 4500$ and $N_1 \sim 2500$ population imbalance is incidental and arises from imperfect state preparation and residual population in nearby levels that are not optically resolved. This mainly reduces the asymmetry fringe contrast, but does not alter the operating principle of the protocol. Note that, as mentioned in the main text, imperfect optical pumping leaves populations in states close in energy to $|0\rangle$ and $|1\rangle$, and the measured N_0 and N_1 include background signals from the population in these nearby states.

The measured asymmetry can be influenced by several effects related to the optical readout process. These can be separated into three mechanisms. First, changes in detection efficiency of each state ($|0\rangle$ and $|1\rangle$) can modify the measured asymmetry. In particular, small variations in the detection laser power can lead to unequal detection efficiencies. In the present experiment, the $|0\rangle \leftrightarrow A$ and $|1\rangle \leftrightarrow A$ transitions are separated by only approximately 60 MHz. To avoid power broadening and spectral overlap, which would significantly reduce the Ramsey fringe contrast, the readout lasers are operated near or below saturation. Operating in this regime increases the susceptibility of the asymmetry to laser power drifts. Moreover, the absolute saturation behavior is difficult to characterize due to possible photon cycling and mixing among excited electronic states, which limits precise knowledge of the relevant transition dipole moments. Note that the transition frequency is extracted from differential measurements in which the electric and/or magnetic fields are switched at approximately 1 Hz and asymmetry differences are taken. This procedure strongly suppresses sensitivity to slow drifts

in detection efficiency and ensures that the extracted frequencies are not biased by such effects at the present level of precision.

To briefly estimate the sensitivity of the asymmetry $\mathcal{A} = (N_0 - N_1)/(N_0 + N_1)$ to changes in detection efficiency, we consider a fractional change $N_0 \to (1 + a)N_0$, yielding

$$\Delta\mathcal{A} \simeq \frac{2N_0N_1}{(N_0 + N_1)^2}a. \tag{A4}$$

For typical values $N_0 \approx 4500$ and $N_1 \approx 2500$, this corresponds to $\Delta\mathcal{A} \approx 0.46a$. Since the typical laser power drift at relevant timescale (1 s) is below 5%, single-shot fluctuations in the asymmetry due to detection-efficiency variations are below those arising from photon shot noise in the total detected signal ($\Delta\mathcal{A} \approx 0.026$). No statistically significant systematic effect associated with this mechanism is observed at the current precision.

Second, population excited to the $A(010)$ state can decay back into the originally addressed state during detection [e.g., $|0\rangle \to A(010) \to |0\rangle$]. This photon cycling contributes to the effective detection efficiency of each state, but does not introduce a qualitatively new bias to the extracted asymmetry or transition frequency beyond a possible modification of the detection efficiency.

Third, decay from the A state can repopulate the other state during detection [e.g., $|0\rangle \to A(010) \to |1\rangle$]. This "cross-talk" process modifies the asymmetry and reduces the observed Ramsey fringe contrast by partially washing out population differences between $|0\rangle$ and $|1\rangle$ [49]. Note that the extracted transition frequencies and field sensitivities do not depend on the Ramsey fringe contrast or assumptions about detailed fringe shape. Although the branching ratio of the decays from the A state is the stable molecular properties which do not depend on experimental parameters, the cross-talk modifies the sensitivity of the measured asymmetry to detection-efficiency fluctuations, which could introduce further bias to the extracted transition frequency. From measurements in which we estimated the cross-talk contributions by comparing photon counts with and without upstream depletion of $|0\rangle$ ($|1\rangle$) prior to the downstream detection of $|1\rangle$ ($|0\rangle$), we find cross-talk at the approximately 10% level, and this does not result in significant change in the sensitivity of the measured asymmetry to detection-efficiency drifts compared with the no-cross-talk case.

For future EDM experiments employing similar readout schemes, these effects must be carefully considered. In particular, operating the detection transitions in a clearly saturated regime where possible, and quantitatively characterizing any detection-efficiency changes and its correlations with experimental switches, will be important for minimizing and bounding associated systematic effects.

3. Extraction of field sensitivities

As mentioned in the main text, we perform Ramsey measurements to conduct Stark and Zeeman spectroscopy and extract the field sensitivities. First, we set the two-photon frequency to lie within the linear portion of the Ramsey fringe (the region highlighted by the orange line in Fig. 5 where the asymmetry varies approximately linearly with two-photon detuning, and the slope is near maximal) and fit the linear portion of the fringe with a linear function to obtain the slope $\mathcal{A}/f$. Next, we vary the fields and record the asymmetries. As an example, we consider two asymmetry data points $\mathcal{A}(\mathcal{E}_0, \mathcal{B}_0)$ and $\mathcal{A}(\mathcal{E}_1, \mathcal{B}_0)$ taken at $\mathcal{E} = \mathcal{E}_0, \mathcal{B} = \mathcal{B}_0$ and $\mathcal{E} = \mathcal{E}_1, \mathcal{B} = \mathcal{B}_0$, respectively, to extract the electric-field sensitivity Δd_{eff}. Note that when we change the applied electric and magnetic fields, we correspondingly choose the two-photon detuning so that it remains on the linear portion of the Ramsey fringe. We then take differences $\mathcal{A}(\mathcal{E}_0, \mathcal{B}_0) - \mathcal{A}(\mathcal{E}_1, \mathcal{B}_0)$ and divide it by the slope $\mathcal{A}/f$ to convert it into a frequency difference $f(\mathcal{E}_0, \mathcal{B}_0) - f(\mathcal{E}_1, \mathcal{B}_0)$. The corresponding fit errors of the slope $\mathcal{A}/f$ are propagated. Finally, this frequency difference is divided by $\mathcal{E}_0 - \mathcal{E}_1$ to obtain the field sensitivity $\Delta d_{\text{eff}}\{[(\mathcal{E}_0 + \mathcal{E}_1)/2], \mathcal{B}_0\} = \{[f(\mathcal{E}_0, \mathcal{B}_0) - f(\mathcal{E}_1, \mathcal{B}_0)]/(\mathcal{E}_0 - \mathcal{E}_1)\}$. We report the field sensitivities at the midpoint $(\mathcal{E}_0 + \mathcal{E}_1/2)$ of two field points ($\mathcal{E}_0$ and $\mathcal{E}_1$), which is valid if the energy shift near the zero-crossing point is quadratic—a behavior that is consistent with both our predictions and the observed data. Nonetheless, around the zero-crossing points, we have $|\mathcal{E}_0 - \mathcal{E}_1| \lesssim 0.5$ V/cm and $|\mathcal{B}_0 - \mathcal{B}_1| \lesssim 0.07$ G. ($|\mathcal{E}_0 - \mathcal{E}_1|$ and

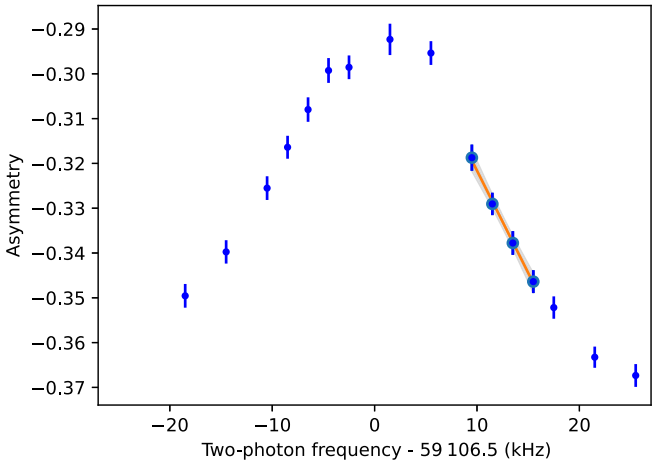

FIG. 5. Ramsey fringe of the EDM-clock transition as a function of the two-photon frequency. The blue points represent measurements, while the orange solid line is a linear fit to the linear portion of the fringe. Error bars denote 1σ standard deviations of repeated asymmetry measurements taken under the same experimental conditions. The shaded regions indicate the uncertainty of the fit. Note that the data here are taken on a different transition and at different field values from Fig. 1(b). The transition in Fig. 1(b) was chosen as an example showing a full fringe.

$|\mathcal{B}_0 - \mathcal{B}_1|$ are different for different data points depending on their frequency shifts.) We repeat this measurement at various electric and magnetic fields to measure the field sensitivities Δd_{eff} and $\Delta\mu_{\text{eff}}$.

The uncertainties in Δd_{eff} and $\Delta\mu_{\text{eff}}$ are obtained by propagating the statistical uncertainties of the measured fluorescence signals. In particular, we repeat the measurements on N_0 and N_1 under certain experimental conditions and take the standard deviation of the resulting distributions as the corresponding statistical uncertainties. These uncertainties are then propagated sequentially from N_0 and N_1 to the asymmetry $\mathcal{A}$, from $\mathcal{A}$ to the extracted transition frequency f, and finally to the field sensitivities Δd_{eff} and $\Delta\mu_{\text{eff}}$, using standard error propagation. As mentioned earlier, the fit uncertainties of the slope $\mathcal{A}/f$ are also propagated. As explained later in Appendix A 5, uncertainties in the electric- and magnetic-field values are likewise propagated and found to be negligible. We assume these uncertainties are uncorrelated.

Note again that, although we show fits of the observed Ramsey fringes to the expected fringe shape in Fig. 1 as a guide to the eye, the extracted transition frequencies and field sensitivities do not depend on assumptions about the detailed fringe shape. The expected Ramsey fringe shape is given by

$$\mathcal{A}(\delta) = \mathcal{C}\frac{\Omega^2}{\Omega_g^2}\sin^2\left(\frac{\Omega_g T}{2}\right)\left[\cos\left(\frac{\Omega_g T}{2}\right)\cos\left(\frac{\delta\tau_{\text{free}}}{2}\right) - \frac{\delta}{\Omega_g}\sin\left(\frac{\Omega_g T}{2}\right)\sin\left(\frac{\delta\tau_{\text{free}}}{2}\right)\right]^2 + A_0, \tag{A5}$$

where $\delta = 2\pi(f - f_{\text{res}})$ is the two-photon detuning, f_{res} is the resonant transition frequency, $\mathcal{C}$ is the Ramsey contrast, τ_{free} is the free evolution time between two pulses, T is the pulse duration, Ω is the two-photon Rabi frequency, $\Omega_g = \sqrt{\Omega^2 + \delta^2}$ is the generalized two-photon Rabi frequency, and $\mathcal{A}_0$ is the asymmetry offset. We incorporate a Gaussian distribution of molecular-beam forward velocities, which leads to a spread in τ_{free} and T. The phase accumulation occurs during the Ramsey pulse as well, so the Ramsey fringe period is $\tau \sim \tau_{\text{free}} + T$ in our case. The fitted values of τ_{free} and T in Fig. 1 are (15 ± 2) and (10 ± 1) μs, respectively. Note that the demonstrated Ramsey free evolution time is currently limited by the available spatial separation between the two Ramsey pulses, which is limited by scattered light from the second Ramsey pulse beam reaching the final detector when it is moved closer to the detection optics. These are technical constraints rather than intrinsic limits of this protocol itself. With improved stray-light suppression and/or modified beam geometry, substantially longer interrogation times should be achievable.

To suppress the effect of any possible drift of the overall asymmetry offset (e.g, due to the drift of the power balance between two frequency components in the fast switching of the detection laser), we alternate the two-photon frequency between the red and blue side of the linear portion of the central Ramsey fringe. By taking the difference of the asymmetries at these two two-photon frequencies, we can cancel out the slow drift of the overall asymmetry offset. For the experimental data where we extract the bounds on the electric- and magnetic-field sensitivities at magic fields (i.e., the data at $\mathcal{E} = 39.60$ V/cm and $\mathcal{B} = 12.15$ G in Fig. 2 in the main text), we have taken additional precautions to measure the frequency shift accurately. First, instead of employing the switch mentioned above, we alternate the two electric- and magnetic-field values around the magic field values. This cancels out the systematic effect more directly. Additionally, although narrowing the detection time window can reduce sensitivity to the velocity spread within a single molecular pulse, it may increase sensitivity to shot-to-shot variations in the overall temporal pulse shape. In particular, changes in the ablation spot on the target could modify the temporal profile and effective exit-time distribution of molecules from the buffer-gas cell, which may imprint on the measured asymmetry. To reduce sensitivity to such pulse-shape variations, we integrate over a larger time window (approximately 4 ms out of approximately 10 ms), at the cost of reduced contrast, though we do not observe conclusive evidence of this effect in the present dataset. Finally, as explained in the next paragraph, we stabilize the two-photon laser power to suppress the effects of laser power drift to well below our measurement uncertainty.

4. Laser power stabilization

For the two-photon transitions, the excitation pulses themselves can cause a frequency shift of the EDM-clock transition (probe-light shift). To investigate this effect, we measure the transition frequency shift via Ramsey measurements at different two-photon laser powers. We change the laser power by 5% with laser power stabilization. The stabilization is done by adjusting the rf amplitude fed into an AOM with an active feedback loop. The measured energy shifts are (0.8 ± 0.8) kHz for the EDM-clock transition and (1.2 ± 0.5) kHz for the field-sensing transition. The laser power drift without power stabilization is typically less than 2% over the experimentally relevant timescale o approximately five to ten minutes. This is the time needed to record a typical approximately 500 shots at one electromagnetic-field point, since the power can be measured and adjusted between field points. Thus, even without active feedback, any frequency shifts arising from laser power drift are smaller than the 1σ errors of this work. Nevertheless, we stabilize the two-photon laser power to make sure the laser power drift (and fluctuation) is well below 1% and thus is negligible for the experimental data

where we extract the bounds on the electric- and magnetic-field sensitivities at magic fields (i.e., the data at $\mathcal{E} = 39.60$ V/cm and $\mathcal{B} = 12.15$ G in Fig. 2 in the main text). Note that the 1σ errors of the switch channel frequency shifts (f^s) shown in Fig. 3 are approximately $2\sqrt{2}$ times smaller than that of the transition frequency shifts $f(\hat{\mathcal{M}}, \hat{\mathcal{E}}|\mathcal{E}|, \hat{\mathcal{B}}|\mathcal{B}|)$ because of the way the switch channels are defined in the main text. Therefore, any possible shift due to the laser power drift is smaller than the 1σ errors shown in Fig. 3 as well. The probe-light ac Stark shift can also be categorized into switch channels and systematically characterized. This effect is well understood and characterized in atomic and molecular clocks, and there are methods to suppress and mitigate it via tailored pulse sequences [63–67] if needed, but also simply by measuring the relationship between laser power and the probe-light shift [27]. Nonetheless, we can make the brief orders of magnitude of the several systematic effects that can arise from the combination of the nonreversing fields and probe-light shifts. To simplify the estimation, we take the typical value of the one-photon detuning $\Delta \sim 2\pi \times 1$ GHz. The relevant probe-light shift for the present measurement is the differential ac Stark shift of the transition, i.e., the difference between the probe-induced light shifts of the upper and lower states. We denote this differential shift by $\Delta f_{\mathrm{LS}}(\Delta)$. The nonreversing fields of $\mathcal{E}_{\mathrm{NR}} \sim 1$ mV/cm and $\mathcal{B}_{\mathrm{NR}} \sim 1$ mG can cause a shift of the one-photon detuning by $\delta \sim 1$ kHz, which correlates with the $\hat{\mathcal{E}}$ and $\hat{\mathcal{B}}$ switches, respectively. For $\delta \ll \Delta$, the resulting switch-correlated change in the differential light shift is, to first order,

$$\delta(\Delta f_{\mathrm{LS}}) \simeq \left| \frac{\partial \Delta f_{\mathrm{LS}}}{\partial \Delta} \right| \delta. \tag{A6}$$

For far-detuned coupling,$\Delta f_{\mathrm{LS}}(\Delta)$ scales approximately as $1/\Delta$, so that

$$\delta(\Delta f_{\mathrm{LS}}) \approx |\Delta f_{\mathrm{LS}}| \frac{\delta}{\Delta}. \tag{A7}$$

Using our experimentally determined bound on the differential probe-light shift $|\Delta f_{\mathrm{LS}}| \lesssim 1$ kHz, we obtain $\delta(\Delta f_{\mathrm{LS}}) \lesssim 1$ mHz.

5. Magnetic fields

A several meter-scale set of square coil pairs outside of the science chamber cancel background magnetic fields down to the approximately mG level in three axes. Another smaller pair of square coils applies a magnetic field of 0–20 G in the Ramsey region along the $\hat{\boldsymbol{Z}}$ axis. We calibrated the magnetic field in the Ramsey measurement region by measuring the Zeeman shift of a magnetically sensitive transition in YbOH using two-photon spectroscopy. The uncertainty in this Zeeman shift measurement was found to be negligible for the final uncertainty of the obtained field sensitivities. Temporal fluctuations of the magnetic and electric fields are roughly 1 mG and 1 mV/cm (on the timescale of a second), respectively, and found to be negligible for the final results.

Transverse fields can arise from misalignments between the electric field, magnetic field, and laser polarization axis. Similar to other EDM experiments [30], these effects do not directly give rise to false EDMs but can couple in at higher orders. Therefore, these effects can also be categorized into switch channels and systematically characterized. To suppress the transverse fields, additional magnetic coils in the $\hat{\boldsymbol{X}}$ and $\hat{\boldsymbol{Y}}$ axes can be installed and magnetic-field stabilization can be applied, as demonstrated elsewhere [68]. The $\hat{\boldsymbol{X}}$- and $\hat{\boldsymbol{Y}}$-axis coils could also be useful for more precise control of the magnetic-field orientation or for the investigation of systematic errors arising from transverse fields.

APPENDIX B: PREDICTION OF TRANSITION PROPERTIES

We previously performed high-resolution spectroscopy on the $\tilde{A}^2\Pi_{1/2}(000) - \tilde{X}^2\Sigma^+(010)$ band in YbOH [17,38] to extract the molecular parameters of the $\tilde{X}^2\Sigma^+(010)$ state. The uncertainties of the measured molecular parameters

TABLE I. Spectroscopic parameters for the $\tilde{X}^2\Sigma^+(010)$ state of YbOH.

Parameter		^{174}YbOH (previous work [38])	^{174}YbOH (adjusted in this work)
T_0/cm^{-1}	Origin energy	319.909 01(6)	319.909 01
B/MHz	Rotation	7328.6(2)	7328.43[a]
γ/MHz	Spin rotation	−88.7(9)	−87.7[a]
γ_G/MHz	Axial spin rotation	16(2)	15.6[a]
q_G/MHz	ℓ doubling	−12.0(2)	−12.2[a]
p_G/MHz	P-odd ℓ doubling	−11(1)	−10.3[a]
$b_F(H)$/MHz	Fermi contact	4.07(18)[b]	4.07[b]
$c(H)$/MHz	Spin dipolar	3.49(38)[b]	3.49[b]
D_{mol}/Debye	Molecular dipole moment	2.16(1)	2.17[a]
g_S	Effective electron g-factor	2.07(2)	2.07[a]

[a]These parameters are manually adjusted in this work to better reproduce the observed field sensitivities.
[b]These parameters are taken from the previous spectroscopy work [62].

were $\lesssim$MHz, which was relatively high compared to the energy scale of Ramsey fringes in this work ($\lesssim$10 kHz). Nevertheless, the theory prediction with the molecular parameters agrees with the properties of EDM-clock transitions explored in this work within the uncertainties, as can be seen from Fig. 2. We can then manually adjust the molecular parameters within their spectroscopic uncertainties to better reproduce the observed field sensitivities. The adjusted molecular parameters used in this work are given in Table I. These parameters were not obtained from a least-squares fit to the present data since the amount of new data points in the present work was not sufficient to fit all the molecular constants. No formal statistical uncertainties are therefore assigned. Note that in the previous work, the hyperfine structure from the distant hydrogen nuclear spin was optically unresolved. Thus, we take the values from the previous two-photon spectroscopy work for the hydrogen hyperfine parameters [Fermi contact term $b_F(H)$ and spin dipolar term $c(H)$] [62].

APPENDIX C: OTHER ENGINEERED TRANSITIONS WITH DIFFERENT FIELD SENSITIVITIES

Besides the EDM-clock transition and field-sensing transition explored in the main text, there are numerous transitions with different sensitivities to the electric field, magnetic field, and eEDM [17]. We have indeed found other transitions experimentally, including ones with suppressed sensitivity to electric fields and high sensitivities to magnetic fields and the eEDM. Figure 6 shows these transitions and their zero crossing of electric-field sensitivity at a magic electric-field value. This electrically insensitive, magnetically sensitive transition may offer an additional set of transitions useful for systematic effect searches. It is worth mentioning that the time-reversed pair of this transition exhibits identical electric-field sensitivity but opposite signs of the eEDM sensitivity. This property is advantageous for systematic error rejection in a small magnetic field (like the case here), which is detailed in our previous publication [17].

APPENDIX D: COMPARISON OF RAMSEY CONTRAST WITH PREDICTIONS

Figure 7 shows the reduction of Ramsey fringe contrast as a function of the electric- and magnetic-field noise amplitude. The noise has uniform distribution with amplitude defined as the difference between the minimum and maximum values. The applied field noise distribution is discretized due to the finite resolution of the current and voltage supply for the magnetic coil and electric-field plate, respectively. For the EDM-clock transition, the applied fields sample 20–1300 discrete values, whereas for the field-sensing transition, the small applied fields sample 2–25 discrete values. For the field-sensing transition, the calculation explicitly includes the discretization of the applied field noise distribution. (For the EDM-clock transition, since the number of the field samples is large, the calculation assumes a continuous noise distribution.) Note that they exhibit a reduced rate of decline at large noise amplitude (e.g., $\gtrsim$1.25 G and $\gtrsim$7 V/cm for the EDM-clock transition) because strong fluctuations distort the original shape of the Ramsey fringe. For the field-sensing transition, the data are plotted on an expanded scale for clarity.

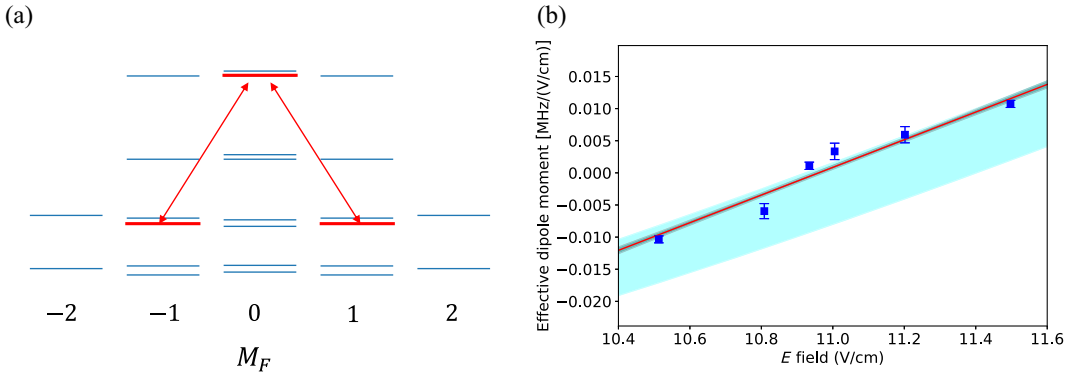

FIG. 6. (a) Level diagrams of the $N'' = 1, \tilde{X}(010)$ state in ^{174}YbOH at $\mathcal{E} = 10.93$ V/cm and $\mathcal{B} = 0$ G, showing an electrically insensitive, magnetically sensitive transition. (b) The electric-field sensitivity as functions of the applied electric fields. We applied an approximately 0.3-G magnetic field to lift the degeneracy between time-reversed pair for demonstration purposes. The electric-field sensitivities are expressed in terms of the effective electric dipole moment. Blue square points represent measurements, the red line is a linear fit, and the shaded gray region indicates the fit uncertainty. Error bars denote 1σ uncertainties in the extracted field sensitivities obtained by the standard error-propagation procedure described in Appendix. A 3. The linear fit yields $(\partial\Delta d_{\mathrm{eff}}/\partial\mathcal{E}) = (21.5 \pm 0.8) \times 10^{-3}$ MHz/(V/cm)^2. The cyan shaded regions indicate the theory uncertainties, which are obtained from the measurement uncertainties of the previous work [38] on the spectroscopic parameters.

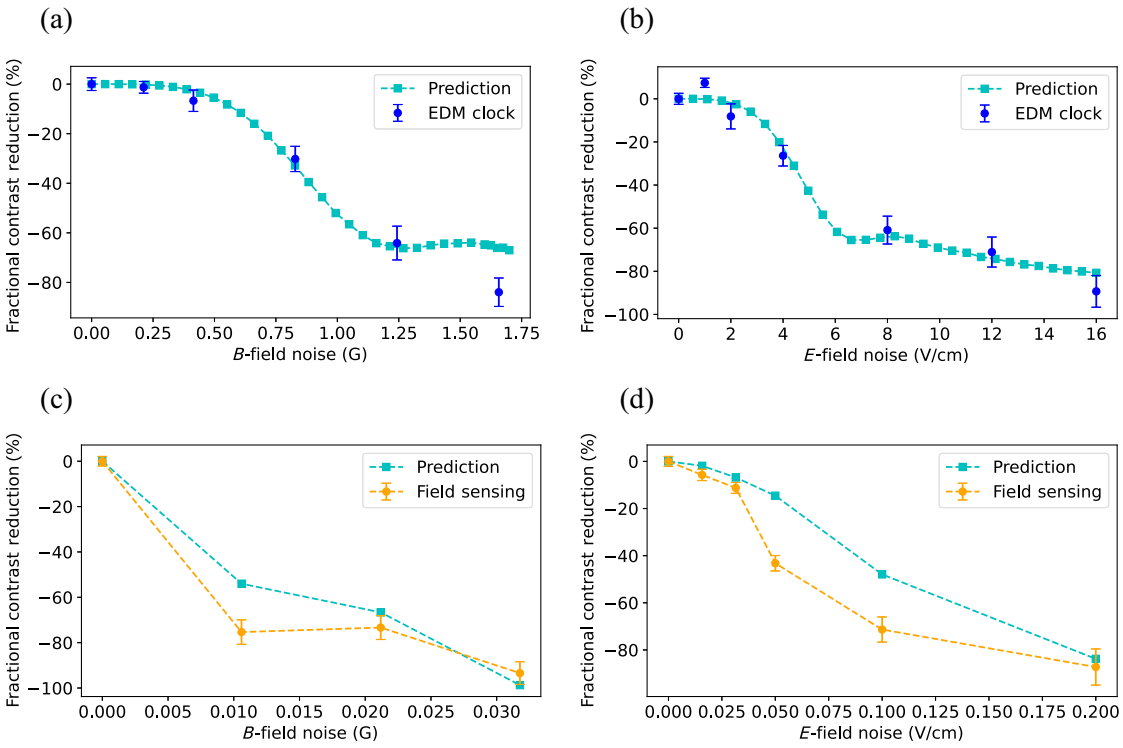

FIG. 7. Reduction in Ramsey fringe contrast as a function of the electric- and magnetic-field noise amplitude. Data in (a) and (c) were taken with zero applied electric field noise, and in (b) and (d) with zero applied magnetic-field noise. The dashed cyan lines indicate the theory predictions. Error bars denote 1σ uncertainties obtained by standard error propagation of the asymmetry difference, where the uncertainty of each asymmetry is taken as the 1σ standard deviation of repeated asymmetry measurements under the same experimental conditions.

APPENDIX E: THE SWITCH CHANNELS

In this section, we present a systematic analysis of switch channels to identify, characterize, and constrain potential systematic effects in the EDM measurement. We first define the switch channels employed in this work and establish the associated notation. We then discuss the expected signatures of both genuine EDM signals and dominant systematic effects in these channels based on symmetry considerations. Using these expectations, we provide order-of-magnitude estimates of relevant systematic effects and describe how corresponding corrections or bounds on them are obtained from the data. Finally, we briefly discuss additional switch channels that are not central to the present analysis but may be useful for future measurements or extended systematic studies.

1. Definitions of the switch channels

The transition frequency $f(\hat{\mathcal{M}},\hat{\mathcal{E}}|\mathcal{E}|,\hat{\mathcal{B}}|\mathcal{B}|)$ is measured under each experimental configuration defined by three binary switches: transition ($\hat{\mathcal{M}}$), electric field ($\hat{\mathcal{E}}$), and magnetic field ($\hat{\mathcal{B}}$). The values of these switches are taken to be ±1 and correspond to the two states of each parameter in which the experiment is operated: two directions of the electric field, two directions of the magnetic field, and two transitions. Here, $\hat{\mathcal{E}}=\mathrm{sign}(\boldsymbol{\mathcal{E}}\cdot\hat{\boldsymbol{Z}}),\hat{\mathcal{B}}=\mathrm{sign}(\boldsymbol{\mathcal{B}}\cdot\hat{\boldsymbol{Z}})$, and $\hat{\mathcal{M}}=+1(-1)$ for the nonmagic field-sensing (magic EDM-clock) transition.

As mentioned in the main text, we form switch channels denoted by f^s, where the superscript s indicates the set of switches for which the quantity is odd under reversal. This is a standard practice for eEDM experiments, and the details can be found in the literature [69], but we summarize the important points and distinctions here. These switch channels are defined as satisfying

$$\begin{aligned} f(\hat{\mathcal{M}},\hat{\mathcal{E}}|\mathcal{E}|,\hat{\mathcal{B}}|\mathcal{B}|) &= f^{(0)}(|\mathcal{E}|,|\mathcal{B}|)+\hat{\mathcal{B}}\hat{f}^{\mathcal{B}}(|\mathcal{E}|,|\mathcal{B}|)+\hat{\mathcal{E}}\hat{f}^{\mathcal{E}}(|\mathcal{E}|,|\mathcal{B}|)\\ &+\hat{\mathcal{M}}\hat{f}^{\mathcal{M}}(|\mathcal{E}|,|\mathcal{B}|)+\hat{\mathcal{M}}\,\hat{\mathcal{B}}\,\hat{f}^{\mathcal{MB}}(|\mathcal{E}|,|\mathcal{B}|)\\ &+\hat{\mathcal{M}}\,\hat{\mathcal{E}}\,\hat{f}^{\mathcal{ME}}(|\mathcal{E}|,|\mathcal{B}|)+\hat{\mathcal{E}}\,\hat{\mathcal{B}}\,\hat{f}^{\mathcal{EB}}(|\mathcal{E}|,|\mathcal{B}|)\\ &+\hat{\mathcal{M}}\,\hat{\mathcal{E}}\,\hat{\mathcal{B}}\,\hat{f}^{\mathcal{MEB}}(|\mathcal{E}|,|\mathcal{B}|). \end{aligned} \tag{E1}$$

This is a convenient parametrization since different phases can be categorized and distinguished by their switch channels. The switch channels depend on $|\mathcal{E}|$ and $|\mathcal{B}|$, but not the switch states $(\hat{\mathcal{M}},\hat{\mathcal{E}},\hat{\mathcal{B}})$, and are calculated from the measurements by sums with either addition or subtraction depending on the switch channel, for example,

$$f^{(0)} = \frac{1}{8}\sum_{\hat{\mathcal{M}},\hat{\mathcal{E}},\hat{\mathcal{B}}} f(\hat{\mathcal{M}},\hat{\mathcal{E}}|\mathcal{E}|,\hat{\mathcal{B}}|\mathcal{B}|), \tag{E2}$$

$$f^{\mathcal{M}} = \frac{1}{8}\sum_{\hat{\mathcal{M}},\hat{\mathcal{E}},\hat{\mathcal{B}}} \hat{\mathcal{M}}\, f(\hat{\mathcal{M}},\hat{\mathcal{E}}|\mathcal{E}|,\hat{\mathcal{B}}|\mathcal{B}|), \tag{E3}$$

$$f^{\mathcal{E}\mathcal{B}} = \frac{1}{8}\sum_{\hat{\mathcal{M}},\hat{\mathcal{E}},\hat{\mathcal{B}}} \hat{\mathcal{E}}\,\hat{\mathcal{B}}\, f(\hat{\mathcal{M}},\hat{\mathcal{E}}|\mathcal{E}|,\hat{\mathcal{B}}|\mathcal{B}|), \tag{E4}$$

$$f^{\mathcal{M}\mathcal{E}\mathcal{B}} = \frac{1}{8}\sum_{\hat{\mathcal{M}},\hat{\mathcal{E}},\hat{\mathcal{B}}} \hat{\mathcal{M}}\,\hat{\mathcal{E}}\,\hat{\mathcal{B}}\, f(\hat{\mathcal{M}},\hat{\mathcal{E}}|\mathcal{E}|,\hat{\mathcal{B}}|\mathcal{B}|) \tag{E5}$$

with the rest defined similarly [30]. Note that here we choose to drop the explicit dependence of switch channels on $|\mathcal{E}|$ and $|\mathcal{B}|$. Standard error propagation of f^s yields

$$\sigma_{f^s} = \frac{1}{8}\sqrt{\sum_{\hat{\mathcal{M}},\hat{\mathcal{E}},\hat{\mathcal{B}}} \sigma^2_{f(\hat{\mathcal{M}},\hat{\mathcal{E}}|\mathcal{E}|,\hat{\mathcal{B}}|\mathcal{B}|)}} \coloneqq \sigma_f. \tag{E6}$$

Here, σ_f is the same for all switch configurations s. Thus, the error of f^s is the same for all switch channels.

2. Expected signatures of systematic effects and EDM signals in switch channels

The transition frequency of any transition depends on electric and magnetic fields due to Stark and Zeeman effects. Since we shall examine the transition frequency of EDM-clock transitions where the first-order linear Stark and Zeeman shifts vanish or become very small, we have to include the dependence of the transition frequency on electric and magnetic fields up to second-order terms. It is worth noting that when we reverse the magnetic field we drive the transition with the different sign of the M_F quantum number if we apply approximately the same frequency, such that the energies derived from the molecular, Stark, and Zeeman Hamiltonian are unchanged. We therefore express

$$\begin{aligned} f(\mathcal{E},\mathcal{B}) &= C_0 + C_{\mathcal{E}}|\mathcal{E}| + C_{\mathcal{B}}|\mathcal{B}| + C_{\mathcal{E}\mathcal{B}}|\mathcal{E}\mathcal{B}| \\ &\quad + C_{\mathcal{E}\mathcal{E}}\mathcal{E}^2 + C_{\mathcal{B}\mathcal{B}}\mathcal{B}^2 \end{aligned} \tag{E7}$$

$$\begin{aligned} &= C_0 + C_{\mathcal{E}}\mathcal{E}\hat{\mathcal{E}} + C_{\mathcal{B}}\mathcal{B}\hat{\mathcal{B}} + C_{\mathcal{E}\mathcal{B}}\mathcal{E}\mathcal{B}\hat{\mathcal{E}}\,\hat{\mathcal{B}} \\ &\quad + C_{\mathcal{E}\mathcal{E}}\mathcal{E}^2 + C_{\mathcal{B}\mathcal{B}}\mathcal{B}^2. \end{aligned} \tag{E8}$$

Here the transition frequency is expanded around some electric and magnetic fields ($\mathcal{E}_0$ and $\mathcal{B}_0$) that are in the vicinity of the electric- and magnetic-field magic points of the EDM-clock transition. C_0 correspond to the transition frequency at $\mathcal{E}_0$ and $\mathcal{B}_0$, and all other coefficients are also given at $\mathcal{E}_0$ and $\mathcal{B}_0$. (Note that here we do not assume the existence of simultaneous zero crossings of both the electric- and magnetic-field sensitivities at a particular electromagnetic-field point.) The absolute values are required to enforce the symmetry that in the absence of imperfections (or CP violation), the transition energy shifts must be even under field reversals. Notice again that when we change the sign of the magnetic field, we are changing the sign of the M_F quantum number if we address a transition with approximately the same frequency, so this symmetry with $\mathcal{B}$ reversal is enforced here unlike in most other eEDM experiments [30]. The symmetry under $\mathcal{E}$ reversal arises from the usual T and P symmetry of the Hamiltonian. These coefficients are determined by fitting to the calculated $\mathcal{E}$ and $\mathcal{B}$ dependence of the transitions around the predicted magic points of the EDM-clock transition and are shown in Table II.

TABLE II. Predicted coefficients in the electromagnetic sensitivities of the EDM-clock transition and field-sensing transition. Note that for these predictions, we use spectroscopic parameters given in Table I, which have larger uncertainties from optical spectroscopy than the experimental energy scale of approximately a few kHz in this work, as explained above. Furthermore, the nuclear spin and rotational Zeeman terms are neglected.

Coefficient	Units	Magic	Nonmagic
$C_{\mathcal{E}}$	kHz/(V/cm)	0	+45.04
$C_{\mathcal{B}}$	kHz/G	0	−197.20
$C_{\mathcal{E}\mathcal{E}}$	kHz/(V/cm)^2	+2.59	+2.61
$C_{\mathcal{B}\mathcal{B}}$	kHz/G^2	+76.91	+73.89
$C_{\mathcal{E}\mathcal{B}}$	kHz/(G × V/cm)	−30.73	−31.19

To include the effects of the state switch $\hat{\mathcal{M}}$, we can define $\bar{C}_{\{\}}$ and $\delta\bar{C}_{\{\}}$ for all of the coefficients as the average and the half of the difference of the parameter $C_{\{\}}$ between the two transitions, respectively. For instance,

$$\bar{C}_{\mathcal{E}} = (C^{\mathrm{FST}}_{\mathcal{E}} + C^{\mathrm{ECT}}_{\mathcal{E}})/2, \quad \delta\bar{C}_{\mathcal{E}} = (C^{\mathrm{FST}}_{\mathcal{E}} - C^{\mathrm{ECT}}_{\mathcal{E}})/2, \tag{E9}$$

and similarly for all other parameters. Here, ECT denotes the EDM-clock transition, and FST denotes the field-sensing transition. Then, the transition frequency can be expressed as

$$\begin{aligned} f(\hat{\mathcal{M}},\mathcal{E},\mathcal{B}) &= (\bar{C}_0 + \hat{\mathcal{M}}\delta\bar{C}_0) + (\bar{C}_{\mathcal{E}} + \hat{\mathcal{M}}\delta\bar{C}_{\mathcal{E}})\mathcal{E}\hat{\mathcal{E}} \\ &\quad + (\bar{C}_{\mathcal{B}} + \hat{\mathcal{M}}\delta\bar{C}_{\mathcal{B}})\mathcal{B}\hat{\mathcal{B}} \\ &\quad + (\bar{C}_{\mathcal{E}\mathcal{B}} + \hat{\mathcal{M}}\delta\bar{C}_{\mathcal{E}\mathcal{B}})\mathcal{E}\mathcal{B}\hat{\mathcal{E}}\,\hat{\mathcal{B}} \\ &\quad + (\bar{C}_{\mathcal{E}\mathcal{E}} + \hat{\mathcal{M}}\delta\bar{C}_{\mathcal{E}\mathcal{E}})\mathcal{E}^2 \\ &\quad + (\bar{C}_{\mathcal{B}\mathcal{B}} + \hat{\mathcal{M}}\delta\bar{C}_{\mathcal{B}\mathcal{B}})\mathcal{B}^2. \end{aligned} \tag{E10}$$

Notice that the field sensitivities defined in the main text are the first derivative of the transition frequency with respect to $\mathcal{E}$ and $\mathcal{B}$,

$$\Delta d_{\text{eff}} = \frac{\partial}{\partial \mathcal{E}} f(\hat{\mathcal{M}}, \mathcal{E}, \mathcal{B}) = (\bar{C}_{\mathcal{E}} + \hat{\mathcal{M}}\delta\bar{C}_{\mathcal{E}}) + (\bar{C}_{\mathcal{EB}} + \hat{\mathcal{M}}\delta\bar{C}_{\mathcal{EB}})\mathcal{B} + 2(\bar{C}_{\mathcal{EE}} + \hat{\mathcal{M}}\delta\bar{C}_{\mathcal{EE}})\mathcal{E}, \tag{E11}$$

$$\Delta\mu_{\text{eff}} = \frac{\partial}{\partial \mathcal{B}} f(\hat{\mathcal{M}}, \mathcal{E}, \mathcal{B}) = (\bar{C}_{\mathcal{B}} + \hat{\mathcal{M}}\delta\bar{C}_{\mathcal{B}}) + (\bar{C}_{\mathcal{EB}} + \hat{\mathcal{M}}\delta\bar{C}_{\mathcal{EB}})\mathcal{E} + 2(\bar{C}_{\mathcal{BB}} + \hat{\mathcal{M}}\delta\bar{C}_{\mathcal{BB}})\mathcal{B}, \tag{E12}$$

and thus their slopes (the second derivative of the transition frequency) are

$$\frac{\partial}{\partial \mathcal{E}}\Delta d_{\text{eff}} = \frac{\partial^2}{\partial^2 \mathcal{E}} f(\hat{\mathcal{M}}, \mathcal{E}, \mathcal{B}) = 2(\bar{C}_{\mathcal{EE}} + \hat{\mathcal{M}}\delta\bar{C}_{\mathcal{EE}}), \tag{E13}$$

$$\frac{\partial}{\partial \mathcal{B}}\Delta\mu_{\text{eff}} = \frac{\partial^2}{\partial^2 \mathcal{B}} f(\hat{\mathcal{M}}, \mathcal{E}, \mathcal{B}) = 2(\bar{C}_{\mathcal{BB}} + \hat{\mathcal{M}}\delta\bar{C}_{\mathcal{BB}}). \tag{E14}$$

The electric and magnetic fields we apply in our experiment can be expressed as $(\mathcal{E}_0 + \Delta\mathcal{E})\hat{\mathcal{E}}$ and $(\mathcal{B}_0 + \Delta\mathcal{B})\hat{\mathcal{B}}$. Here, $\Delta\mathcal{E}$ and $\Delta\mathcal{B}$ are the displacements of the fields from $\mathcal{E}_0$ and $\mathcal{B}_0$. There are also nonreversing fields, which result in field magnitudes that change upon nominal reversal. Thus, the actual total fields we apply ($\mathcal{E}$ and $\mathcal{B}$) are the sum of ($\mathcal{E}_0\hat{\mathcal{E}}$ and $\mathcal{B}_0\hat{\mathcal{B}}$), displacements ($\Delta\mathcal{E}\hat{\mathcal{E}}$ and $\Delta\mathcal{B}\hat{\mathcal{B}}$) and nonreversing fields ($\mathcal{E}_{\text{NR}}$ and $\mathcal{B}_{\text{NR}}$), and we can therefore express the fields as

$$\mathcal{E} = \mathcal{E}_0\hat{\mathcal{E}} + \Delta\mathcal{E}\hat{\mathcal{E}} + \mathcal{E}_{\text{NR}}, \tag{E15}$$

$$\mathcal{B} = \mathcal{B}_0\hat{\mathcal{B}} + \Delta\mathcal{B}\hat{\mathcal{B}} + \mathcal{B}_{\text{NR}}. \tag{E16}$$

For clarity, we now focus only on systematic errors arising from nonreversing electric and magnetic fields, $\mathcal{E}_{\text{NR}}$ and $\mathcal{B}_{\text{NR}}$, which are some of the most common and important cases. As mentioned in the main text, other imperfections, such as field gradients or transverse components introduced by misalignment of the electric field, magnetic field, and laser-polarization axes, can also produce systematic errors. The significance of these additional imperfections depends on specific details of each experiment, and any future precision measurement must examine and suppress them carefully and thoroughly. In some cases, our protocol offers sensitive electric- and magnetic-field probes to assist these investigations [40]. Importantly, a range of EDM-clock transitions and field-sensing transitions with different sensitivities to different imperfections can be selected to diagnose and mitigate these systematic errors.

Finally, we can include the eEDM shift $d_e\mathcal{E}_{\text{eff}}\hat{\mathcal{E}}\,\hat{\mathcal{B}}$. Similar to the considerations needed for the Stark and Zeeman shifts, the eEDM shift here is manifestly $\mathcal{E}$ and $\mathcal{B}$ odd since reversal of $\mathcal{B}$ also effectively means reversal of M_F and therefore the eEDM shift. We can understand this in the following way. First, the state-dependent molecular orientation $\hat{\boldsymbol{n}}$ follows the applied electric-field direction like $\hat{\boldsymbol{n}} = \hat{\mathcal{E}}\,\hat{\boldsymbol{Z}}$. Second, we also have $\hat{\boldsymbol{S}} = \text{sign}(M_F)$, and M_F is the projection of the total angular momentum along the $\hat{\boldsymbol{Z}}$ axis. Again, the magnetic-field reversal means M_F reversal, and therefore we have $\hat{\boldsymbol{S}} = \hat{\mathcal{B}}\,\hat{\boldsymbol{Z}}$. Finally, the Hamiltonian for the eEDM term is $d_e\mathcal{E}_{\text{eff}}\hat{\boldsymbol{S}}\cdot\hat{\boldsymbol{n}} = d_e\mathcal{E}_{\text{eff}}\hat{\mathcal{E}}\,\hat{\mathcal{B}}$.

Using these parametrizations, and including the eEDM shift, we can build a table of the switch channels.

For convenience, we can simplify these expressions with new notation. Notice that $f^{\mathcal{B}}$ and $f^{\mathcal{MB}}$ are proportional to $\mathcal{B}_{\text{NR}}$. Since the EDM-clock field sensitivities are much smaller than that of the field-sensing transition, we have that $\bar{C}_{\{\}} \approx \delta C_{\{\}}$ [see Eq. (E 2)] for the various field-sensitivity coefficients. This sensitivity to $\mathcal{B}_{\text{NR}}$ is therefore similar for these two channels, so we define $f^{\mathcal{B}} = \mathcal{B}_{\text{NR}}\mu_{\text{eff}}$ and $f^{\mathcal{MB}} = \mathcal{B}_{\text{NR}}\mu_{\text{eff}}$ where $\mu_{\text{eff}} = (\bar{C}_{\mathcal{B}} + \Delta\mathcal{E}\bar{C}_{\mathcal{EB}} + 2\Delta\mathcal{B}\bar{C}_{\mathcal{BB}}) \approx (\delta C_{\mathcal{B}} + \Delta\mathcal{E}\delta C_{\mathcal{EB}} + 2\Delta\mathcal{B}\delta C_{\mathcal{BB}})$. Very similarly, we can define $f^{\mathcal{E}} = \mathcal{E}_{\text{NR}}d_{\text{eff}}$ and $f^{\mathcal{ME}} = \mathcal{E}_{\text{NR}}d_{\text{eff}}$ where $d_{\text{eff}} = (\bar{C}_{\mathcal{E}} + \Delta\mathcal{B}\bar{C}_{\mathcal{EB}} + 2\Delta\mathcal{E}\bar{C}_{\mathcal{EE}}) \approx (\delta C_{\mathcal{E}} + \Delta\mathcal{B}\delta C_{\mathcal{EB}} + 2\Delta\mathcal{E}\delta C_{\mathcal{EE}})$. We can thus further simplify the table.

For the specific pair of transitions considered in the main text, the two transitions have the same $\mathcal{E}_{\text{eff}}$ to within 4%, so $\bar{\mathcal{E}}_{\text{eff}} \approx \mathcal{E}_{\text{eff}}$ and $\delta\bar{\mathcal{E}}_{\text{eff}} \approx 0$. Therefore, we regard $f^{\mathcal{EB}}$ as the "eEDM channel." Other transitions could be chosen with different relative eEDM sensitivity, providing further systematic checks of the eEDM channels.

3. Estimates and corrections of systematic effects

As can be seen from Tables III and IV, $\mathcal{E}_{\text{NR}}$ and $\mathcal{B}_{\text{NR}}$ contribute to eEDM channel $f^{\mathcal{EB}} = \bar{C}_{\mathcal{EB}}\mathcal{E}_{\text{NR}}\mathcal{B}_{\text{NR}}$ and also to $f^{\mathcal{ME}} = d_{\text{eff}}\mathcal{E}_{\text{NR}}$ and $f^{\mathcal{MB}} = \mu_{\text{eff}}\mathcal{B}_{\text{NR}}$. Thus, $f^{\mathcal{ME}}$ and $f^{\mathcal{MB}}$ serve as sensitive probes of $\mathcal{E}_{\text{NR}}$ and $\mathcal{B}_{\text{NR}}$, respectively, with much larger sensitivities than the eEDM channel $f^{\mathcal{EB}}$. The direct nonreversing field systematic error can be expressed in more experimentally relevant units as $\bar{C}_{\mathcal{EB}} \approx 30\ \mu\text{Hz}/(\mu\text{G} \times \text{mV/cm})$, or

TABLE III. A table of switch channels in the general case.

Channel	Terms
$f^{(0)}$	$\Delta\mathcal{B}\bar{C}_{\mathcal{B}} + \mathcal{B}_{\text{NR}}^2\bar{C}_{\mathcal{BB}} + \Delta\mathcal{B}^2\bar{C}_{\mathcal{BB}} + \Delta\mathcal{E}\bar{C}_{\mathcal{E}} + \Delta\mathcal{B}\Delta\mathcal{E}\bar{C}_{\mathcal{EB}} + \Delta\mathcal{E}^2\bar{C}_{\mathcal{EE}} + \mathcal{E}_{\text{NR}}^2\bar{C}_{\mathcal{EE}}$
$f^{\mathcal{B}}$	$\mathcal{B}_{\text{NR}}\bar{C}_{\mathcal{B}} + 2\mathcal{B}_{\text{NR}}\Delta\mathcal{B}\bar{C}_{\mathcal{BB}} + \mathcal{B}_{\text{NR}}\Delta\mathcal{E}\bar{C}_{\mathcal{EB}}$
$f^{\mathcal{E}}$	$\mathcal{E}_{\text{NR}}\bar{C}_{\mathcal{E}} + \Delta\mathcal{B}\mathcal{E}_{\text{NR}}\bar{C}_{\mathcal{EB}} + 2\Delta\mathcal{E}\mathcal{E}_{\text{NR}}\bar{C}_{\mathcal{EE}}$
$f^{\mathcal{EB}}$	$\mathcal{B}_{\text{NR}}\mathcal{E}_{\text{NR}}\bar{C}_{\mathcal{EB}} + d_e\bar{\mathcal{E}}_{\text{eff}}$
$f^{\mathcal{M}}$	$\Delta\mathcal{B}\delta C_{\mathcal{B}} + \mathcal{B}_{\text{NR}}^2\delta C_{\mathcal{BB}} + \Delta\mathcal{B}^2\delta C_{\mathcal{BB}} + \Delta\mathcal{E}\delta C_{\mathcal{E}} + \Delta\mathcal{B}\Delta\mathcal{E}\delta C_{\mathcal{EB}} + \Delta\mathcal{E}^2\delta C_{\mathcal{EE}} + \mathcal{E}_{\text{NR}}^2\delta C_{\mathcal{EE}}$
$f^{\mathcal{MB}}$	$\mathcal{B}_{\text{NR}}\delta C_{\mathcal{B}} + 2\mathcal{B}_{\text{NR}}\Delta\mathcal{B}\delta C_{\mathcal{BB}} + \mathcal{B}_{\text{NR}}\Delta\mathcal{E}\delta C_{\mathcal{EB}}$
$f^{\mathcal{ME}}$	$\mathcal{E}_{\text{NR}}\delta C_{\mathcal{E}} + \Delta\mathcal{B}\mathcal{E}_{\text{NR}}\delta C_{\mathcal{EB}} + 2\Delta\mathcal{E}\mathcal{E}_{\text{NR}}\delta C_{\mathcal{EE}}$
$f^{\mathcal{MEB}}$	$\mathcal{B}_{\text{NR}}\mathcal{E}_{\text{NR}}\delta C_{\mathcal{EB}} + d_e\delta\mathcal{E}_{\text{eff}}$

TABLE IV. A simplified table of switch channels.

Channel	Terms
$f^{(0)}$	$\Delta\mathcal{B}\bar{C}_{\mathcal{B}} + \mathcal{B}_{\mathrm{NR}}^2\bar{C}_{\mathcal{BB}} + \Delta\mathcal{B}^2\bar{C}_{\mathcal{BB}} + \Delta\mathcal{E}\bar{C}_{\mathcal{E}} + \Delta\mathcal{B}\Delta\mathcal{E}\bar{C}_{\mathcal{EB}} + \Delta\mathcal{E}^2\bar{C}_{\mathcal{EE}} + \mathcal{E}_{\mathrm{NR}}^2\bar{C}_{\mathcal{EE}}$
$f^{\mathcal{B}}$	$\mathcal{B}_{\mathrm{NR}}\mu_{\mathrm{eff}}$
$f^{\mathcal{E}}$	$\mathcal{E}_{\mathrm{NR}}d_{\mathrm{eff}}$
$f^{\mathcal{EB}}$	$\mathcal{B}_{\mathrm{NR}}\mathcal{E}_{\mathrm{NR}}\bar{C}_{\mathcal{EB}} + d_e\bar{\mathcal{E}}_{\mathrm{eff}}$
$f^{\mathcal{M}}$	$\Delta\mathcal{B}\delta C_{\mathcal{B}} + \mathcal{B}_{\mathrm{NR}}^2\delta C_{\mathcal{BB}} + \Delta\mathcal{B}^2\delta C_{\mathcal{BB}} + \Delta\mathcal{E}\delta C_{\mathcal{E}} + \Delta\mathcal{B}\Delta\mathcal{E}\delta C_{\mathcal{EB}} + \Delta\mathcal{E}^2\delta C_{\mathcal{EE}} + \mathcal{E}_{\mathrm{NR}}^2\delta C_{\mathcal{EE}}$
$f^{\mathcal{MB}}$	$\mathcal{B}_{\mathrm{NR}}\mu_{\mathrm{eff}}$
$f^{\mathcal{ME}}$	$\mathcal{E}_{\mathrm{NR}}d_{\mathrm{eff}}$
$f^{\mathcal{MEB}}$	$\mathcal{B}_{\mathrm{NR}}\mathcal{E}_{\mathrm{NR}}\delta\bar{C}_{\mathcal{EB}} + d_e\delta\bar{\mathcal{E}}_{\mathrm{eff}}$

$d_{e,\mathrm{false}} \approx 6\times10^{-30}\ e\,\mathrm{cm}/(\mu\mathrm{G}\times\mathrm{mV/cm})$. It is worth noting that $\bar{C}_{\mathcal{EB}}$ is a parameter that depends only on molecular transition properties (but not experimental properties) and can be determined straightforwardly and independently from the slope measurements of switch channels such as $f^{\mathcal{EB}}/\mathcal{E}_{\mathrm{NR}}$ and $f^{\mathcal{EB}}/\mathcal{B}_{\mathrm{NR}}$, for example, by direct Stark and Zeeman measurements. This allows us to distinguish between the direct nonreversing field systematic error and the systematic errors arising from the complicated higher-order effects like nonreversing fields coupling to laser effects, if present.

Importantly, one can correct the false eEDM contribution by using the other channels $Q = \bar{C}_{\mathcal{EB}}\mathcal{E}_{\mathrm{NR}}\mathcal{B}_{\mathrm{NR}} = \bar{C}_{\mathcal{EB}}/(d_{\mathrm{eff}}\mu_{\mathrm{eff}})f^{\mathcal{ME}}f^{\mathcal{MB}}$. Here, $d_e\bar{\mathcal{E}}_{\mathrm{eff}} = f^{\mathcal{EB}} - Q$. When the field sensitivities and coefficients are determined with relative uncertainties of $\sigma_{d_{\mathrm{eff}}}/d_{\mathrm{eff}}, \sigma_{\mu_{\mathrm{eff}}}/\mu_{\mathrm{eff}}, \sigma_{\bar{C}_{\mathcal{EB}}}/\bar{C}_{\mathcal{EB}} < \sigma_f/f^{\mathcal{ME}}, \sigma_f/f^{\mathcal{MB}}$, error propagation yields

$$\sigma_Q = Q\sqrt{\left(\frac{\sigma_f}{f^{\mathcal{ME}}}\right)^2 + \left(\frac{\sigma_f}{f^{\mathcal{MB}}}\right)^2 + \left(\frac{\sigma_{\bar{C}_{\mathcal{EB}}}}{\bar{C}_{\mathcal{EB}}}\right)^2 + \left(\frac{\sigma_{d_{\mathrm{eff}}}}{d_{\mathrm{eff}}}\right)^2 + \left(\frac{\sigma_{\mu_{\mathrm{eff}}}}{\mu_{\mathrm{eff}}}\right)^2 + \frac{2\sigma_{\mathcal{EB}}}{f^{\mathcal{ME}}f^{\mathcal{MB}}}} \tag{E17}$$

$$< Q\sqrt{\left(\frac{\sigma_f}{f^{\mathcal{ME}}}\right)^2 + \left(\frac{\sigma_f}{f^{\mathcal{MB}}}\right)^2 + \left(\frac{\sigma_{\bar{C}_{\mathcal{EB}}}}{\bar{C}_{\mathcal{EB}}}\right)^2 + \left(\frac{\sigma_{d_{\mathrm{eff}}}}{d_{\mathrm{eff}}}\right)^2 + \left(\frac{\sigma_{\mu_{\mathrm{eff}}}}{\mu_{\mathrm{eff}}}\right)^2 + \frac{2\sigma_f^2}{f^{\mathcal{ME}}f^{\mathcal{MB}}}} \tag{E18}$$

$$\sim Q\sqrt{\left(\frac{\sigma_f}{f^{\mathcal{ME}}}\right)^2 + \left(\frac{\sigma_f}{f^{\mathcal{MB}}}\right)^2 + \frac{2\sigma_f^2}{f^{\mathcal{ME}}f^{\mathcal{MB}}}} \tag{E19}$$

$$= \frac{\bar{C}_{\mathcal{EB}}}{d_{\mathrm{eff}}\mu_{\mathrm{eff}}}\sqrt{(f^{\mathcal{ME}}f^{\mathcal{MB}}\sigma_f)^2\left\{\left(\frac{1}{f^{\mathcal{ME}}}\right)^2 + \left(\frac{1}{f^{\mathcal{MB}}}\right)^2 + \frac{2}{f^{\mathcal{ME}}f^{\mathcal{MB}}}\right\}} \tag{E20}$$

$$= \frac{\bar{C}_{\mathcal{EB}}}{d_{\mathrm{eff}}\mu_{\mathrm{eff}}}\sqrt{(f^{\mathcal{ME}})^2 + (f^{\mathcal{MB}})^2 + 2f^{\mathcal{ME}}f^{\mathcal{MB}}}\sigma_f \tag{E21}$$

$$\sim 8\times10^{-6}\left[\frac{1}{\mathrm{Hz}}\right]\sqrt{(f^{\mathcal{ME}})^2 + (f^{\mathcal{MB}})^2 + 2f^{\mathcal{ME}}f^{\mathcal{MB}}}\sigma_f \tag{E22}$$

$$\ll \sigma_f. \tag{E23}$$

Thus, σ_Q is suppressed compared to σ_f. Here, in Eq. (22), we use $f^{\mathcal{MB}}, f^{\mathcal{ME}} \ll 100$ kHz. In Eq. (17), $\sigma_{\mathcal{EB}}$ is the covariance of $f^{\mathcal{ME}}$ and $f^{\mathcal{MB}}$, and follows

$$\begin{aligned}\sigma_{\mathcal{EB}} = \frac{1}{64}\Big(&\sigma^2_{f(+1,+|\mathcal{E}|,+|\mathcal{B}|)} - \sigma^2_{f(+1,+|\mathcal{E}|,-|\mathcal{B}|)} - \sigma^2_{f(+1,-|\mathcal{E}|,+|\mathcal{B}|)} + \sigma^2_{f(+1,-|\mathcal{E}|,-|\mathcal{B}|)} \\ &+ \sigma^2_{f(-1,+|\mathcal{E}|,+|\mathcal{B}|)} - \sigma^2_{f(-1,+|\mathcal{E}|,-|\mathcal{B}|)} - \sigma^2_{f(-1,-|\mathcal{E}|,+|\mathcal{B}|)} + \sigma^2_{f(-1,-|\mathcal{E}|,-|\mathcal{B}|)}\Big) \\ &< \frac{1}{64}\sum_{\hat{\mathcal{M}},\hat{\mathcal{E}},\hat{\mathcal{B}}}\sigma^2_{f(\hat{\mathcal{M}},\hat{\mathcal{E}}|\mathcal{E}|,\hat{\mathcal{B}}|\mathcal{B}|)} = \sigma_f^2,\end{aligned} \tag{E24}$$

or simply,

TABLE V. A table of measured (Meas) slopes with errors (Err) and predictions (Pred) for the different switch parity channels versus both $\mathcal{E}_{\mathrm{NR}}$ and $\mathcal{B}_{\mathrm{NR}}$. The numbers in parentheses indicate prediction uncertainties from the spectroscopic parameter uncertainties.

	Slope vs $\mathcal{E}_{\mathrm{NR}}$			Slope vs $\mathcal{B}_{\mathrm{NR}}$		
Channel	Pred	Meas	Err	Pred	Meas	Err
$f^{(0)}$	0	+2.6	1.5	0	−0.61	6.4
$f^{\mathcal{B}}$	0	+1.3	1.5	−99(39)	−66	6.4
$f^{\mathcal{E}}$	+22(11)	+14	1.5	0	+6.0	6.4
$f^{\mathcal{EB}}$	0	+2.5	1.5	0	+0.96	6.4
$f^{\mathcal{M}}$	0	+0.72	1.5	0	−2.1	6.4
$f^{\mathcal{MB}}$	0	+1.1	1.5	−99(39)	−66	6.4
$f^{\mathcal{ME}}$	+22(11)	+17	1.5	0	−6.1	6.4
$f^{\mathcal{MEB}}$	0	−0.83	1.5	0	+1.3	6.4
Units		Hz/(mV/cm)			Hz/mG	

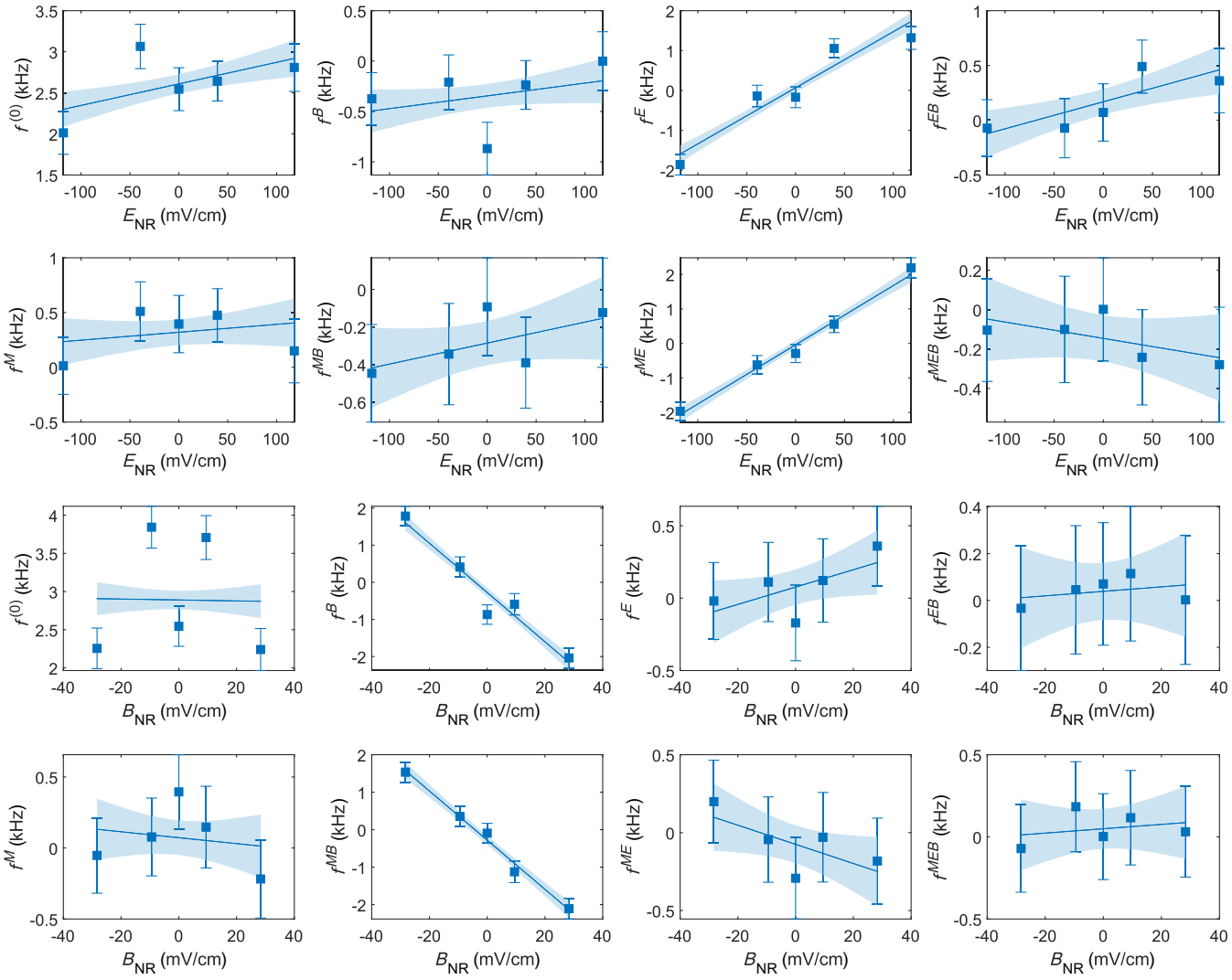

FIG. 8. A plot of all switch parity channels vs nonreversing fields. Error bars denote 1σ uncertainties in the extracted frequency shifts obtained by the standard error-propagation procedure described in Appendix. A 3. Note that the (0) channel is susceptible to overall drifts and is therefore expected to be noisy [70].

$$\sigma_{\mathcal{EB}} = \rho_{\mathcal{EB}}\sigma_{f^{\mathcal{ME}}}\sigma_{f^{\mathcal{MB}}} = \rho_{\mathcal{EB}}\sigma_f^2 \ll \sigma_f^2, \tag{E25}$$

where $\rho_{\mathcal{EB}}$ is the correlation between $f^{\mathcal{ME}}$ and $f^{\mathcal{MB}}$ and satisfies $-1 \le \rho \le 1$. We define covariance between $f^{\mathcal{EB}}$ and Q as $\sigma_{\mathcal{EB}Q}$ and its magnitude satisfies the following:

$$\sigma_{\mathcal{EB}Q} = \rho\sigma_{f^{\mathcal{EB}}}\sigma_Q = \rho\sigma_f\sigma_Q \le \sigma_f\sigma_Q \ll \sigma_f^2, \tag{E26}$$

where ρ is, again, the correlation between $f^{\mathcal{EB}}$, and Q and satisfies $-1 \le \rho \le 1$. Thus, the uncertainty of the term $d_e\bar{\mathcal{E}}_{\text{eff}}$ is dominated by the uncertainty of $f^{\mathcal{EB}}$, σ_f.

The high suppression of $\bar{C}_{\mathcal{EB}}/(d_{\text{eff}}\mu_{\text{eff}})$ relies on the high field sensitivities of the field-sensing transition on the order of Δd_{typ} and $\Delta\mu_{\text{typ}}$, and therefore is a general feature of field-sensing transitions. The result shows that switching between EDM-clock transitions and field-sensing transitions serves as a robust protocol against systematic effects induced by nonreversing fields. This systematic error correction protocol is very similar to that of the HfF^+ experiment [40], which has effectively suppressed systematic errors arising from these effects. Note again that all the possible additional systematic shifts in $f^{\mathcal{MB}}$, $f^{\mathcal{ME}}$, and $f^{\mathcal{EB}}$ must be thoroughly explored to measure and place limits on them, which can be assisted by our sensing channels such as $f^{\mathcal{ME}}$ and $f^{\mathcal{MB}}$, similar to the HfF^+ experiment [40]. Again, a range of EDM-clock transitions and field-sensing transitions with different sensitivities to different imperfections could further assist in the investigation of the systematic errors. The field-sensing transition here is chosen purely for its experimental accessibility; however, other field-sensing transitions with different eEDM and field sensitivities can be used if desired.

4. Other switch channels

Other channels such as $f^{\mathcal{E}}, f^{\mathcal{B}}, f^{\mathcal{MEB}}$ also provide information on $\mathcal{E}_{\text{NR}}$, $\mathcal{B}_{\text{NR}}$, and the eEDM, offering an extra cross-check of the eEDM signal and its associated systematics, which can be seen from Fig. 8. Here, $f^{\mathcal{E}}$ and $f^{\mathcal{B}}$ also show sharp linear responses to $\mathcal{E}_{\text{NR}}$ and $\mathcal{B}_{\text{NR}}$ with fitted slopes of $\Delta\bar{d}_{\text{eff}} = 14.1 \pm 1.5\ \text{kHz}/(\text{V/cm}) \sim \delta\Delta d_{\text{eff}}$ and $\Delta\bar{\mu}_{\text{eff}} = -66.3 \pm 6.4\ \text{kHz/G} \sim \delta\Delta\mu_{\text{eff}}$, respectively, thereby serving as another independent probe of $\mathcal{E}_{\text{NR}}$ and $\mathcal{B}_{\text{NR}}$. A table of measured slopes with errors and predictions for the different switch parity channels versus both $\mathcal{E}_{\text{NR}}$ and $\mathcal{B}_{\text{NR}}$ is given in Table V.

[1] S. L. Cornish, M. R. Tarbutt, and K. R. A. Hazzard, *Quantum computation and quantum simulation with ultracold molecules*, Nat. Phys. **20**, 730 (2024).

[2] T. Karman, M. Tomza, and J. Pérez-Ríos, *Ultracold chemistry as a testbed for few-body physics*, Nat. Phys. **20**, 722 (2024).

[3] D. DeMille, N. R. Hutzler, A. M. Rey, and T. Zelevinsky, *Quantum sensing and metrology for fundamental physics with molecules*, Nat. Phys. **20**, 741 (2024).

[4] O. P. Sushkov and V. V. Flambaum, *Parity breaking effects in diatomic molecules*, Sov. Phys. JETP **48**, 608 (1978).

[5] M. S. Safronova, D. Budker, D. DeMille, Derek F. Jackson Kimball, A. Derevianko, and C. W. Clark, *Search for new physics with atoms and molecules*, Rev. Mod. Phys. **90**, 025008 (2018).

[6] N. R. Hutzler, *Polyatomic molecules as quantum sensors for fundamental physics*, Quantum Sci. Technol. **5**, 044011 (2020).

[7] T. S. Roussy, L. Caldwell, T. Wright, W. B. Cairncross, Y. Shagam, K. B. Ng, N. Schlossberger, S. Y. Park, A. Wang, J. Ye, and E. A. Cornell, *An improved bound on the electron's electric dipole moment*, Science **381**, 46 (2023).

[8] V. Andreev, D. G. Ang, D. DeMille, J. M. Doyle, G. Gabrielse, J. Haefner, N. R. Hutzler, Z. Lasner, C. Meisenhelder, B. R. O'Leary, C. D. Panda, A. D. West, E. P. West, and X. Wu, *Improved limit on the electric dipole moment of the electron*, Nature (London) **562**, 355 (2018).

[9] R. Stutz and E. Cornell, *Search for the electron EDM using trapped molecular ions*, Bull. Am. Phys. Soc. **89**, 76 (2004).

[10] D. DeMille, F. Bay, S. Bickman, D. Kawall, D. Krause, S. E. Maxwell, and L. R. Hunter, *Investigation of PbO as a system for measuring the electric dipole moment of the electron*, Phys. Rev. A **61**, 052507 (2000).

[11] R. Alarcon *et al.*, *Electric dipole moments and the search for new physics*, arXiv:2203.08103.

[12] T. A. Isaev and R. Berger, *Polyatomic candidates for cooling of molecules with lasers from simple theoretical concepts*, Phys. Rev. Lett. **116**, 063006 (2016).

[13] I. Kozyryev, L. Baum, K. Matsuda, and J. M. Doyle, *Proposal for laser cooling of complex polyatomic molecules*, ChemPhysChem **17**, 3641 (2016).

[14] N. Fitch and M. Tarbutt, *Laser-cooled molecules*, Adv. At. Mol. Opt. Phys. **70**, 157 (2021).

[15] F. J. Collings, N. J. Fitch, R. A. Jenkins, J. M. Dyne, E. Wursten, M. T. Ziemba, X. S. Zheng, F. Castellini, J. Lim, B. E. Sauer, and M. R. Tarbutt, *Low-noise environment for probing fundamental symmetries*, New J. Phys. **27**, 105004 (2025).

[16] O. Grasdijk, O. Timgren, J. Kastelic, T. Wright, S. Lamoreaux, D. DeMille, K. Wenz, M. Aitken, T. Zelevinsky, T. Winick, and D. Kawall, *CeNTREX: A new search for time-reversal symmetry violation in the 205 Tl nucleus*, Quantum Sci. Technol. **6**, 044007 (2021).

[17] Y. Takahashi, C. Zhang, A. Jadbabaie, and N. R. Hutzler, *Engineering field-insensitive molecular clock transitions for symmetry violation searches*, Phys. Rev. Lett. **131**, 183003 (2023).

[18] M. Verma, A. M. Jayich, and A. C. Vutha, *Electron electric dipole moment searches using clock transitions in ultracold molecules*, Phys. Rev. Lett. **125**, 153201 (2020).

[19] C. Ho, J. Lim, B. Sauer, and M. Tarbutt, *Measuring the nuclear magnetic quadrupole moment in heavy polar molecules*, Front. Phys. **11**, 1086980 (2023).

[20] L. Anderegg, N. B. Vilas, C. Hallas, P. Robichaud, A. Jadbabaie, J. M. Doyle, and N. R. Hutzler, *Quantum control of trapped polyatomic molecules for eEDM searches*, Science **382**, 665 (2023).

[21] A. Derevianko and H. Katori, *Colloquium: Physics of optical lattice clocks*, Rev. Mod. Phys. **83**, 331 (2011).

[22] A. D. Ludlow, M. M. Boyd, J. Ye, E. Peik, and P. O. Schmidt, *Optical atomic clocks*, Rev. Mod. Phys. **87**, 637 (2015).

[23] H. Kim, H. S. Han, and D. Cho, *Magic polarization for optical trapping of atoms without stark-induced dephasing*, Phys. Rev. Lett. **111**, 243004 (2013).

[24] I. Ushijima, M. Takamoto, and H. Katori, *Operational magic intensity for sr optical lattice clocks*, Phys. Rev. Lett. **121**, 263202 (2018).

[25] S. Kotochigova and D. DeMille, *Electric-field-dependent dynamic polarizability and state-insensitive conditions for optical trapping of diatomic polar molecules*, Phys. Rev. A **82**, 063421 (2010).

[26] S. Burchesky, L. Anderegg, Y. Bao, S. S. Yu, E. Chae, W. Ketterle, K.-K. Ni, and J. M. Doyle, *Rotational coherence times of polar molecules in optical tweezers*, Phys. Rev. Lett. **127**, 123202 (2021).

[27] K. H. Leung, B. Iritani, E. Tiberi, I. Majewska, M. Borkowski, R. Moszynski, and T. Zelevinsky, *Terahertz vibrational molecular clock with systematic uncertainty at the* 10^{-14} *level*, Phys. Rev. X **13**, 011047 (2023).

[28] A. Aeppli, K. Kim, W. Warfield, M. S. Safronova, and J. Ye, *Clock with* 8×10^{-19} *systematic uncertainty*, Phys. Rev. Lett. **133**, 023401 (2024).

[29] M. Denis, Pi A. B. Haase, Rob G. E. Timmermans, E. Eliav, N. R. Hutzler, and A. Borschevsky, *Enhancement factor for the electric dipole moment of the electron in the BaOH and YbOH molecules*, Phys. Rev. A **99**, 042512 (2019).

[30] J. Baron, W. C. Campbell, D. DeMille, J. M. Doyle, G. Gabrielse, Y. V. Gurevich, P. W. Hess, N. R. Hutzler, E. Kirilov, I. Kozyryev, B. R. O'Leary, C. D. Panda, M. F. Parsons, B. Spaun, A. C. Vutha, A. D. West, and E. P. West, *Methods, analysis, and the treatment of systematic errors for the electron electric dipole moment search in thorium monoxide*, New J. Phys. **19**, 073029 (2017).

[31] I. Kozyryev and N. R. Hutzler, *Precision measurement of time-reversal symmetry violation with laser-cooled polyatomic molecules*, Phys. Rev. Lett. **119**, 133002 (2017).

[32] T. S. Roussy, D. A. Palken, W. B. Cairncross, B. M. Brubaker, D. N. Gresh, M. Grau, K. C. Cossel, K. B. Ng, Y. Shagam, Y. Zhou, V. V. Flambaum, K. W. Lehnert, J. Ye, and E. A. Cornell, *Experimental constraint on axionlike particles over seven orders of magnitude in mass*, Phys. Rev. Lett. **126**, 171301 (2021).

[33] M. Fan, B. Nima, A. Radak, G. Alonso-Álvarez, and A. Vutha, *Wideband search for axionlike dark matter using octupolar nuclei in a crystal*, Phys. Rev. Lett. **136**, 121802 (2026).

[34] K. Gaul and R. Berger, *Ab initio study of parity and time-reversal violation in laser-coolable triatomic molecules*, Phys. Rev. A **101**, 012508 (2020).

[35] V. V. Flambaum, D. DeMille, and M. G. Kozlov, *Time-reversal symmetry violation in molecules induced by nuclear magnetic quadrupole moments*, Phys. Rev. Lett. **113**, 103003 (2014).

[36] E. Kirilov, W. C. Campbell, J. M. Doyle, G. Gabrielse, Y. V. Gurevich, P. W. Hess, N. R. Hutzler, B. R. O'Leary, E. Petrik, B. Spaun, A. C. Vutha, and D. DeMille, *Shot-noise-limited spin measurements in a pulsed molecular beam*, Phys. Rev. A **88**, 013844 (2013).

[37] A. Petrov and A. Zakharova, *Sensitivity of the YbOH molecule to P,T-odd effects in an external electric field*, Phys. Rev. A **105**, L050801 (2022).

[38] A. Jadbabaie, Y. Takahashi, N. H. Pilgram, C. J. Conn, Y. Zeng, C. Zhang, and N. R. Hutzler, *Characterizing the fundamental bending vibration of a linear polyatomic molecule for symmetry violation searches*, New J. Phys. **25**, 073014 (2023).

[39] H. Loh, K. C. Cossel, M. C. Grau, K.-K. Ni, E. R. Meyer, J. L. Bohn, J. Ye, and E. A. Cornell, *Precision spectroscopy of polarized molecules in an ion trap*, Science **342**, 1220 (2013).

[40] L. Caldwell, T. S. Roussy, T. Wright, W. B. Cairncross, Y. Shagam, K. B. Ng, N. Schlossberger, S. Y. Park, A. Wang, J. Ye, and E. A. Cornell, *Systematic and statistical uncertainty evaluation of the* hff^+ *electron electric dipole moment experiment*, Phys. Rev. A **108**, 012804 (2023).

[41] X. Wu, Z. Han, J. Chow, D. G. Ang, C. Meisenhelder, C. D. Panda, E. P. West, G. Gabrielse, J. M. Doyle, and D. DeMille, *The metastable* Q3Δ2 *state of ThO: A new resource for the ACME electron EDM search*, New J. Phys. **22**, 023013 (2020).

[42] N. H. Pilgram, A. Jadbabaie, Y. Zeng, N. R. Hutzler, and T. C. Steimle, *Fine and hyperfine interactions in* ^{171}YbOH *and* ^{173}YbOH, J. Chem. Phys. **154**, 244309 (2021).

[43] T. Chen, C. Zhang, L. Cheng, K. B. Ng, S. Malbrunot-Ettenauer, V. V. Flambaum, Z. Lasner, J. M. Doyle, P. Yu, C. J. Conn, C. Zhang, N. R. Hutzler, A. M. Jayich, B. Augenbraun, and D. DeMille, *Relativistic exact two-component coupled-cluster study of molecular sensitivity factors for nuclear schiff moments*, J. Phys. Chem. A **128**, 6540 (2024). pMID: 39047199.

[44] K. C. Stuntz, K. L. Rice, L. Cheng, and B. L. Augenbraun, *Optical cycling and sensitivity to the electron's electric dipole moment in gold-containing molecules*, Phys. Rev. A **110**, 042807 (2024).

[45] A. Sunaga, Y. Takahashi, A. Vutha, and Y. Takahashi, *Measuring the nuclear magnetic quadrupole moment of optically trapped ytterbium atoms in the metastable state*, New J. Phys. **26**, 023023 (2024).

[46] B. L. Augenbraun, Z. D. Lasner, A. Frenett, H. Sawaoka, C. Miller, T. C. Steimle, and J. M. Doyle, *Laser-cooled polyatomic molecules for improved electron electric dipole moment searches*, New J. Phys. **22**, 022003 (2020).

[47] X. Alauze, J. Lim, M. A. Trigatzis, S. Swarbrick, F. J. Collings, N. J. Fitch, B. E. Sauer, and M. R. Tarbutt, *An ultracold molecular beam for testing fundamental physics*, Quantum Sci. Technol. **6**, 044005 (2021).

[48] N. J. Fitch, J. Lim, E. A. Hinds, B. E. Sauer, and M. R. Tarbutt, *Methods for measuring the electron's electric dipole moment using ultracold ybf molecules*, Quantum Sci. Technol. **6**, 014006 (2020).

[49] R. A. Jenkins, M. T. Ziemba, F. J. Collings, X. S. Zheng, F. Castellini, E. Wursten, J. Lim, B. E. Sauer, and M. R. Tarbutt, *Spin interferometry in a beam of ultracold molecules*, arXiv:2602.00713.

[50] E. Fraval, M. J. Sellars, and J. J. Longdell, *Method of extending hyperfine coherence times in* Pr^{3+}*:* Y_2SiO_5, Phys. Rev. Lett. **92**, 077601 (2004).

[51] M. Fan, B. Nima, A. Radak, G. Alonso-Álvarez, and A. Vutha, *First results from a search for axionlike dark*

matter using octupole-deformed nuclei in a crystal, arXiv: 2410.02218.

[52] A. Marc, M. Hubert, and T. Fleig, *Candidate molecules for next-generation searches of hadronic charge-parity violation*, Phys. Rev. A **108**, 062815 (2023).

[53] M. Śmiałkowski and M. Tomza, *Highly polar molecules consisting of a copper or silver atom interacting with an alkali-metal or alkaline-earth-metal atom*, Phys. Rev. A **103**, 022802 (2021).

[54] M. Löw, M. Ibrügger, G. Rempe, and M. Zeppenfeld, *Coherence of symmetry-protected rotational qubits in cold polyatomic molecules*, Phys. Rev. Lett. **134**, 113402 (2025).

[55] C. Zhang, P. Yu, A. Jadbabaie, and N. R. Hutzler, *Quantum-enhanced metrology for molecular symmetry violation using decoherence-free subspaces*, Phys. Rev. Lett. **131**, 193602 (2023).

[56] K. Najafian, Z. Meir, and S. Willitsch, *From megahertz to terahertz qubits encoded in molecular ions: Theoretical analysis of dipole-forbidden spectroscopic transitions in* N_2^+, Phys. Chem. Chem. Phys. **22**, 23083 (2020).

[57] A. Prehn, M. Ibrügger, G. Rempe, and M. Zeppenfeld, *High-resolution "magic"-field spectroscopy on trapped polyatomic molecules*, Phys. Rev. Lett. **127**, 173602 (2021).

[58] Y. Takahashi, H. D. Ramachandran, A. Jadbabaie, Y. Zeng, C. Zhang, and N. R. Hutzler, *Data supporting the figures and analysis in "Engineered Molecular Clock Transitions for Precision Measurements,"* https://github.com/YuikiTakahashi/Yuiki_Takahashi_magic_demonstration_data_PRX_2026 (2026) (accessed: 2026-05-03).

[59] A. Jadbabaie, N. H. Pilgram, J. Klos, S. Kotochigova, and N. R. Hutzler, *Enhanced molecular yield from a cryogenic buffer gas beam source via excited state chemistry*, New J. Phys. **22**, 022002 (2020).

[60] N. R. Hutzler, H.-I. Lu, and J. M. Doyle, *The buffer gas beam: An intense, cold, and slow source for atoms and molecules.*, Chem. Rev. **112**, 4803 (2012).

[61] Y. Takahashi, D. Shlivko, G. Woolls, and N. R. Hutzler, *Simulation of cryogenic buffer gas beams*, Phys. Rev. Res. **3**, 023018 (2021).

[62] A. Jadbabaie, *Measuring fundamental symmetry violation in polyatomic molecules*, Ph. D. thesis, California Institute of Technology, 2023.

[63] R. Santra, E. Arimondo, T. Ido, C. H. Greene, and J. Ye, *High-accuracy optical clock via three-level coherence in neutral bosonic* ^{88}Sr, Phys. Rev. Lett. **94**, 173002 (2005).

[64] T. Zanon-Willette, A. D. Ludlow, S. Blatt, M. M. Boyd, E. Arimondo, and J. Ye, *Cancellation of stark shifts in optical lattice clocks by use of pulsed raman and electromagnetically induced transparency techniques*, Phys. Rev. Lett. **97**, 233001 (2006).

[65] A. V. Taichenachev, V. I. Yudin, C. W. Oates, Z. W. Barber, N. D. Lemke, A. D. Ludlow, U. Sterr, C. Lisdat, and F. Riehle, *Compensation of field-induced frequency shifts in ramsey spectroscopy of optical clock transitions*, JETP Lett. **90**, 713 (2010).

[66] V. I. Yudin, A. V. Taichenachev, C. W. Oates, Z. W. Barber, N. D. Lemke, A. D. Ludlow, U. Sterr, C. Lisdat, and F. Riehle, *Hyper-Ramsey spectroscopy of optical clock transitions*, Phys. Rev. A **82**, 011804(R) (2010).

[67] R. Hobson, W. Bowden, S. A. King, P. E. G. Baird, I. R. Hill, and P. Gill, *Modified hyper-ramsey methods for the elimination of probe shifts in optical clocks*, Phys. Rev. A **93**, 010501(R) (2016).

[68] Z.-X. Duan, W.-T. Wu, Y.-T. Lin, and S.-J. Yang, *Simple and active magnetic-field stabilization for cold atom experiments*, Rev. Sci. Instrum. **93**, 123201 (2022).

[69] J. Baron, W. C. Campbell, D. DeMille, J. M. Doyle, G. Gabrielse, Y. V. Gurevich, P. W. Hess, N. R. Hutzler, E. Kirilov, I. Kozyryev, B. R. O'Leary, C. D. Panda, M. F. Parsons, E. S. Petrik, B. Spaun, A. C. Vutha, and A. D. West, *Order of magnitude smaller limit on the electric dipole moment of the electron*, Science **343**, 269 (2014).

[70] N. R. Hutzler, *A new limit on the electron electric dipole moment*, Ph.D. thesis, Harvard University, 2014.